Mixed Domains Enhance Charge Generation and Extraction in Bulk-Heterojunction Solar Cells with Small-Molecule Donors

Obaid Alqahtani, Maxime Babics, Julien Gorenflot, Victoria Savikhin, Thomas Ferron, Ahmed H. Balawi, Andreas Paulke, Zhipeng Kan, Michael Pope, Andrew J. Clulow, Jannic Wolf, Paul L. Burn, Ian R. Gentle, Dieter Neher, Michael F. Toney, Frédéric Laquai, Pierre M. Beaujuge,* Brian A. Collins**

Keywords: Small molecule, organic solar cell, photovoltaic device, charge transport, domain purity, mixed domains, resonant X-ray scattering, microscopy, transient spectroscopy.

The interplay between nanomorphology and efficiency of polymer-fullerene bulk-heterojunction (BHJ) solar cells has been the subject of intense research, but the generality of these concepts for small-molecule (SM) BHJs remains unclear. Here, the relation between performance, charge generation, recombination, and extraction dynamics and nanomorphology, achievable with two analogous benzo[1,2-*b*:4,5-*b*]dithiophene-pyrido[3,4-*b*]-pyrazine SM donors (BDT(PPTh$_2$)$_2$, namely SM1 and SM2, differing by their side-chain substitution pattern, are examined as a function of solution additive composition. The results show that 1,8-diiodooctane (DIO), used as a processing additive acts as a plasticizer in the blends, increases domain size, and promotes ordering/crystallinity. Surprisingly, the system with high domain purity (SM1) exhibits both poor exciton harvesting and severe charge trapping, alleviated only slightly with increased crystallinity. In contrast, the system consisting of mixed domains and lower crystallinity (SM2) shows both excellent exciton harvesting and low charge recombination losses. Importantly, the onset of large, highly-ordered pure crystallites in the latter (SM2) system reduces solar cell efficiency, pointing to possible differences in the ideal morphologies for SM-based BHJ solar cells compared with polymer-fullerene devices. In polymer-based systems, tie chains between pure polymer crystals establish a continuous charge transport network, whereas SM-based active layers may in some cases require mixed domains at concentrations that enable both small molecule aggregation and charge percolation to the electrodes.

1. Introduction

Organic photovoltaic devices (OPVs) continue to represent an exciting prospect for solar to electrical power generation. Being comprised of earth-abundant and potentially non-toxic materials, OPVs can be manufactured by scalable solution-based fabrication techniques such as roll-to-roll coating or ink-jet printing. Progress in the field has resulted in efficiencies >13%,[1] with a predicted achievable efficiency of 20% –a firm target.[2–6] BHJ OPV devices based on well-defined, π-conjugated SM electron donors have recently reached efficiencies that rival their more widely studied polymer-fullerene BHJ solar cell counterparts.[7,8,90] An advantage of SMs over polymers is that their well-defined, monodisperse architectures enable facile purification, reproducible syntheses, and ease of scalability for commercialization and use in large-area PV modules. SMs have also been demonstrated to have increased molecular ordering compared with polymers,[9–11] which can lead to improved charge mobilities, higher quantum efficiencies, and lower energy losses after photoabsorption.[12] Thus, SM BHJ solar cells provide a plausible route to achieving predicted efficiencies.

With the development of new material systems for "donor-acceptor" BHJ solar cells (active layers comprising at least one electron-donor and one electron-acceptor component), research has increasingly focused on determining the ideal active layer nanomorphology to enhance device performance. Through this effort on polymer-fullerene cells, several guidelines have emerged such as the need for ~10 nm domains to enable efficient exciton harvesting and, more recently, the presence of pure domains of each molecule for higher charge mobility and suppressed recombination.[13–17] It is not sufficient for the materials in the BHJ to have appropriate energy levels, but it is also critical that the film morphology is optimized. Small molecules have different constraints and properties than polymers, and for SM-based OPVs to realize their full potential, morphological guidelines must be developed

O. Alqahtani, T. Ferron, M. Pope, Prof. B. A. Collins
Dept. Physics and Astronomy, Washington State University, Pullman, WA, 99164, USA, Email: brian.collins@wsu.edu
M. Babics, Dr. J. Gorenflot, A. Balawi, Dr. Z. Kan, Prof. F. Laquai, Prof. P. M. Beaujuge
King Abdullah University of Science and Technology (KAUST), KAUST Solar Center, Physical Sciences and Engineering Division, Material Science and Engineering Program, Thuwal, 23955-6900, Saudia Arabia
V. Savikhin, Prof. M. F. Toney
Stanford Synchrotron Radiation Lightsource, SLAC National Accelerator Laboratory, Menlo Park, CA 94025, USA
Dr. A. Paulke, Prof. D. Neher
Institut fur Physik und Astronomie, Physik weicher Materie, University of Potsdam, Potsdam-Golm 14476, Germany
Dr. A. J. Clulow, Prof. P. L. Burn, Prof. I. R. Gentle
Centre for Organic Photonics & Electronics, The University of Queensland, Queensland, 4072, Australia

that take into account these differences. Only recently has initial work focused on general relationships between morphology and performance for SM systems.[17,91]

In recent work, we expanded the range of wide-bandgap ($E_g > 1.8eV$) SM donor materials for BHJ solar cells through the design and synthesis of a SM system that achieved efficiencies as high as 6.5% when blended with the fullerene acceptor $PC_{71}BM$.[18] The molecules were derived from the alternating push-pull motif that has been used in the low-bandgap SM donor p-DTS$(BTTh_2)_2$,[19,20] replacing the dithienosilole-benzothiadiazole (DTS-BT) moiety with a benzo[1,2-*b*:4,5-*b*']dithiophene-pyrido[3,4-*b*]pyrazine (BDT-PP) core and yielding an analogue with deeper HOMO and shallower LUMO levels, namely BDT$(PPTh_2)_2$ (see Table S1 for levels). The BDT unit is common to several high-performing polymer systems,[21] while the PP unit is more synthetically tunable than BT and can include alkyl side-chains that contribute toward solubility. Our initial study involved four analogous BDT$(PPTh_2)_2$ donors with distinct side-chain patterns, resulting in BHJ solar cells with very different morphologies and performance figures despite the donor molecules having similar π-conjugated main-chains, energy levels, and optical gaps.[18]

Such distinct efficiency figures obtained across a set of structurally analogous SM donors –differing only by their side-chain substitution pattern– represent an opportunity to examine how their substituents influence the development of thin-film nanostructures and how nanostructures impact device efficiency in SM BHJ solar cells. Thus, two of the better-performing molecules were selected for further investigation, namely SM1 and SM2 shown in **Figure 1a**. Notably, the BDT motifs in SM1 bear alkoxy side-chain substituents, whereas BDT units in SM2 are appended with alkyl-substituted thiophene pendant groups (so-called "ring substituents"). Both SM donors possess relatively large optical gaps (~1.8-1.9 eV,[18] similar to that of P3HT[22]) compared with the lower optical gap of the p-DTS$(BTTh_2)_2$ counterpart (~1.5 eV),[20] making them of particular interest for use as UV absorbers in tandem solar cells or semitransparent device applications.[23]

In our initial work, we found that adding small quantities of the additive DIO to the chlorobenzene (CB) processing solvent was key in enhancing device performance. Solvent additives like DIO are often used to influence film morphology, leading to an alteration of both the local packing structure and the mesoscale domain morphology (size, composition, and connectivity between domains). Their effects are as of yet difficult to predict for a particular pair of molecules. Reports exist of additives enhancing[24–26] or reducing[27,28] aggregation as well as coarsening[26,29,30] or dispersing[31,32] domains. These morphological changes have been attributed to several possible mechanisms, including the additive acting as a differential solvent (solvating one molecule while the other solidifies),[33] being a better solvent than the processing solvent (controlling solution preaggregation),[27,34] suppressing liquid-liquid phase separation,[35] and acting as a plasticizer (enabling phase evolution and crystallization after evaporation of the processing solvent).[33,36–38] In our initial work with BDT$(PPTh_2)_2$ analogues, transmission electron microscopy (TEM) measurements could not resolve quantitative changes imparted to the mesoscale morphology of the BHJ active layers processed under various conditions.[18] Thus, little is known to date on what causes the dramatic increase in device performance in these systems when DIO is added to the solution.

In this contribution, we examine the performance, charge generation, recombination and extraction dynamics, and nanomorphology formation in BHJ solar cells fabricated with the two BDT$(PPTh_2)_2$ analogues SM1 and SM2 in the presence (and absence) of DIO additive in the blend solution. We find that, at low concentrations, DIO acts as a plasticizer, increasing domain size and ordering in a similar trend as that reported earlier for DTS$(BTTh_2)_2$.[37,38] However, above a critical DIO concentration threshold, a high degree of crystallinity forms across the active layer. The lower miscibility between SM1 and $PC_{71}BM$ results in large, nearly pure domains, even without DIO, leading to exciton recombination and charge trapping. When DIO is added to the blend, the crystallinity of the film increases, and significant charge trapping and recombination still occurs. In contrast, the high miscibility of SM2 with $PC_{71}BM$ results in small, mixed domains, with the BHJ films exhibiting high exciton harvesting and low charge recombination that is optimized at low levels of crystallinity. For SM2, device performance is further improved by using DIO through increased local aggregation and molecular alignment measured within *and between* domains embedded in a molecularly mixed matrix. Such a result suggests that different target morphologies are likely needed in SM donor-based BHJ solar cells compared to those of their polymer-fullerene counterparts, *i.e.*, a higher level of mixing for efficient charge generation and percolation due to the lack of polymer tie chains.

2. Results

2.1. Device Performance

Solar cell devices (area: 0.1 cm^2) with the structure Glass/ITO/MoO_x/SM:$PC_{71}BM$/Ca/Al were fabricated with active layers (all 90±5 nm thick) cast from 1:1 blends (by weight) dissolved in chlorobenzene with 0, 0.2, or 0.5 liquid volume percent (v.%) DIO. Concentrations up to 1 v.% were also used but produced lower efficiencies and are not discussed here. Device performance was assessed under AM1.5G solar illumination, and the *J-V* curves are provided in **Figure 1. Table 1** gives a summary of the performance parameters obtained for the various conditions examined. As reported in our initial work,[18] the two SM donors achieved optimized device

performance for different concentrations of DIO additive (0.5 v.% for SM1 devices vs 0.2 v.% for SM2 devices), but the use of DIO led to an overall solar cell efficiency improvement in both cases.

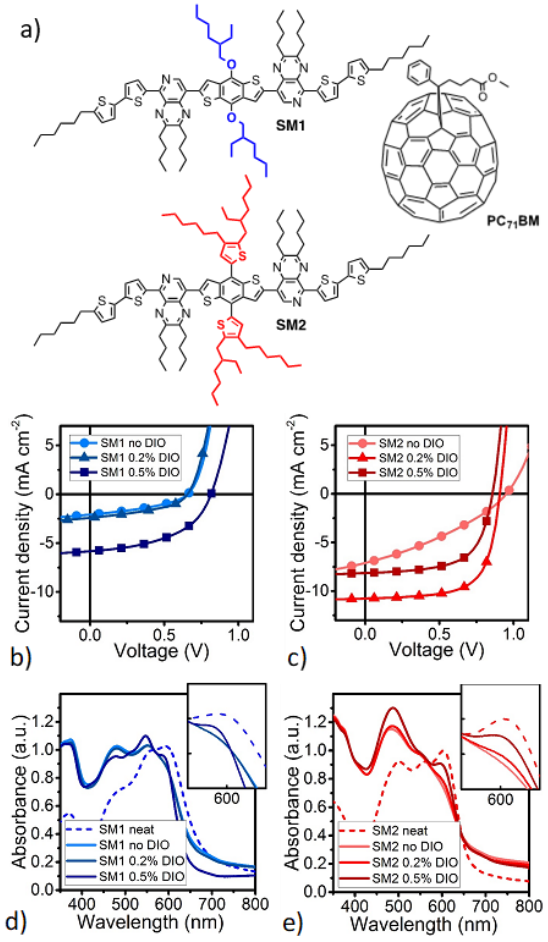

Figure 1. (a) Molecular structure of the benzo[1,2-*b*:4,5-*b′*]dithiophene-pyrido[3,4-*b*]-pyrazine SM donor analogues (BDT($PPTh_2$)$_2$; **SM1** and **SM2**) used in the study, along with that of the fullerene acceptor $PC_{71}BM$. (b) Characteristic *J-V* curves of SM1:$PC_{71}BM$ solar cells fabricated with different DIO concentration (c) Characteristic *J-V* curves of SM2:$PC_{71}BM$ solar cells fabricated with different DIO concentration (d) thin-film UV-Vis absorption spectra (normalized) for neat SM1 (dashed) and blended with $PC_{71}BM$ (solid) (e) thin-film UV-Vis absorption spectra (normalized) for neat SM2 (dashed) and blended with $PC_{71}BM$ (solid)

The different trends in device performance vs. DIO concentration -despite the structural molecular similarity of the SM donors- is important to note. SM1–based cells exhibit a substantial rise in J_{SC} and V_{OC} only when a DIO concentration of 0.5 v.% is employed (little-to-no improvement for lower concentrations), corresponding to the best device performance measured. The *FF* increases monotonically with DIO concentration. The performance trends for SM2-based cells are different from that of the SM1-based devices. When adding only 0.2 v.% DIO, the device efficiency more than doubles, with significant increases in J_{SC} and *FF*, which then reverse course beyond 0.5 v.% DIO concentrations. V_{OC}, on the other hand, decreases monotonically with increasing DIO concentrations. While very different, both behaviors indicate the presence of multiple effects, and competing influences on charge generation and extraction when DIO is employed as the processing additive.

Table 1. Device performance and photoluminescence quenching (PLQ) efficiency from SM (1 or 2):$PC_{71}BM$ ratio of 1:1 (wt/wt) solution-cast from chlorobenzene (CB) with the indicated amounts of DIO additive.

SM	DIO	J_{sc}	V_{oc}	FF	Avg. PCE[a)]	Max. PCE	PLQ
	[v.%]	[mA/cm²]	[V]	[%]	[%]	[%]	[%]
1	0	2.1	0.66	36	0.5	0.7	89.9
	0.2	2.4	0.66	42	0.7	0.8	88.0
	0.5[b)]	5.7	0.81	49	2.3	2.5	45.5
2	0	7.0	0.95	36	2.4	2.6	99.3
	0.2[b)]	10.5	0.90	67	6.3	6.5	99.1
	0.5	8.2	0.86	62	4.4	4.5	88.5

[a)]Additional device statistics, including standard deviations, are provide in Table S1 in the Supporting Information; [b)]optimized amount of DIO.

The normalized absorbance spectra of the six different active layers and neat SM donor films cast without DIO reveal trends on the SM donor aggregation state. The insets of **Figure 1d** and **1e** emphasizes the aggregation peak at *ca.* 600 nm. The presence of $PC_{71}BM$ reduces the intensity of this peak for all devices relative to the neat films, indicating that the fullerene disrupts the aggregation of the SM donor. For the SM1–based blends, spectra for 0 v.% and 0.2 v.% DIO are identical, and only with 0.5 v.% DIO does aggregation become more pronounced. These observations follow the trend in device performance parameters discussed above. On the other hand, the aggregation-related absorption features of SM2 in the blend increase monotonically with the amount of DIO additive. This trend does not follow that of the device performance, and requires a more in-depth study of the charge generation process and the morphological changes occurring across the active layer with various concentrations of DIO.

2.2. Dynamics of Charge Generation

The device metrics are all affected by several fundamental processes associated with the conversion of photons (light) into extracted electrons (photocurrent). We thus turn to a stepwise characterization of the charge generation and collection processes in these devices by employing steady-state and transient spectroscopy techniques. With absorption being nearly identical for all devices (SM1 systematically absorbs slightly more light than SM2 from 540-600nm, see **Figure S1**), we focus on the four main subsequent processes: exciton dynamics, charge generation, charge recombination, and charge extraction. This provides more insight into the reasons for the observed performance trends – particularly the differences in J_{SC} and *FF*.

2.2.1 Exciton Dynamics

Photoluminescence quenching (PLQ) efficiencies are summarized in **Table 1**. Such data is an effective ceiling on the efficiency of converting excitons into charges. Of note is that PLQ for both systems decreases when DIO is added to the casting solution. In the case of the SM2 system, the reduction in PLQ is initially insignificant with >99% of radiative recombination channels quenched with 0 v.% or 0.2 v.% DIO, the latter representing optimized processing conditions. Increasing DIO further to 0.5 v.% reduced the PLQ to <90%. The SM1 system is quite different with ~90% PLQ reduced to <50% under 'device optimized' DIO concentrations. This indicates that fewer than half of all excitons created (photons absorbed) are available for charge generation. Such a significant reduction in PLQ is unexpected considering the drastic improvement of device performance.

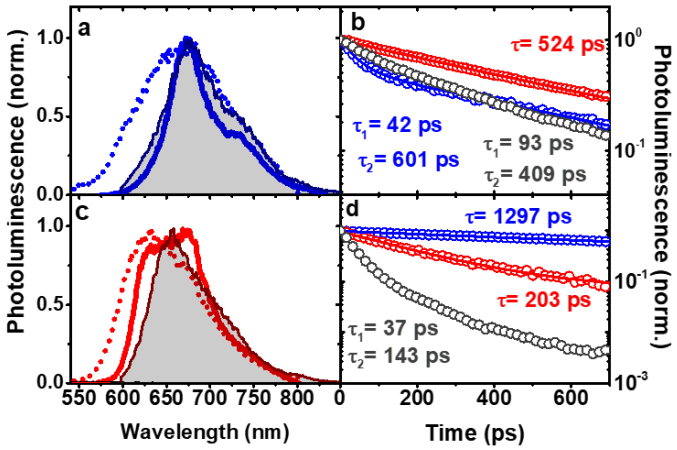

Figure 2. Normalized photoluminescence (PL) spectra averaged between 0 and 200 ps of (a) SM1 and (c) SM2 in chlorobenzene solution (dotted lines) and in neat films (solid lines). The differences at short wavelength are attributed to self-absorption in the dense film. The normalized PL spectra of the corresponding blends are overlaid as grey-shaded area curves. The films, both neat and blends, were prepared with the optimal DIO concentration (0.5 v.% for SM1 and 0.2 v.% for SM2). (b) and (d): corresponding normalized decays of the PL intensity of solutions (blue), neat films (red), and that of blend films (black).

To gain further insight into exciton diffusion, we monitored their dynamics by time-resolved (TRPL) and steady-state photoluminescence spectroscopy. These (see **Figure 2**) experiments provided several important insights: first, a certain degree of molecular order observed in neat SM1 and SM2 films is disrupted in DIO-optimized thin-film blends, an observation that is even more evident for SM2. Second, excitons in SM1 and SM2 films exhibit very different diffusion characteristics to quenching sites (such as defects for neat films or heterojunction interfaces in case of the blends).

The existence of molecular order in thin films of pure SM1 and SM2 is inferred from the increased vibronic structure of the PL compared to that of the molecules in chlorobenzene solution. The broad spectra in solution point to a distribution of molecular conformations. In the case of SM1, this is supported by a change from bi-exponential PL dynamics in solution to mono-exponential dynamics in neat films (see inset of **Figure 2a**) consistent with a more homogeneous molecular environment in films and the absence of structural relaxation. As indicated by the weaker vibrational structure of the PL spectra of optimal blends (grey areas in **Figure 2**), this molecular order is significantly reduced in blends versus the neat film.

Turning to the dynamics (insets of **Figure 2**), one would expect a shorter PL lifetime in films than in solutions due to exciton diffusion to quenching sites (defects or boundaries, for instance) in films, which facilitate recombination. Interestingly, films of SM1 appear to not follow this principle: the PL lifetime in neat films of SM1 (524 ps) remains similar to the longer-lived component observed in solution (bi-exponential decay yielding 601 ps and 42 ps time constants). This remains valid even upon blending SM1 with $PC_{71}BM$ (optimal DIO) as only a limited fraction (31%) of the PL exhibited a fast decay component, estimated to have a lifetime of 93 ps, while most of the PL decay remained similar (409 ps) to that of the neat films of SM1 (524 ps), consistent with the poor PLQ. This indicates that the average distance to defects (in the neat film) or to the interface with the electron acceptor (in blends) tends to be larger than the exciton diffusion length, which in turn points to either slow exciton diffusion or a large average distance to quenching sites. In contrast, SM2 neat films showed significantly shorter PL lifetimes (203 ps) compared to those observed on isolated molecules in solution (1297 ps) (see inset of **Figure 2b**). In optimized SM2 blend films, the PL decay components (37 ps and 143 ps) are substantially shorter than those of the neat films of SM2 (here 85% of the PL decay is associated to the shorter time constant), indicating that a majority of the exciton population reached the interface within the average diffusion length. As further described below, we believe this difference between SM1 and SM2 blend film PL lifetimes is due to the presence of larger and more pure SM1 phases in optimal SM1:$PC_{71}BM$ blends.

2.2.2 Charge Generation

The diffusion-limited exciton dissociation in optimized SM1 blends results in poorer charge generation yields than optimized SM2 blends, as evidenced by transient absorption (TA) pump-probe spectroscopy experiments. **Figure 3a** and **3b** show the blend TA spectra at selected delay times (continuous lines) as well as the spectra of neat SM1 and SM2 films at early delay times (dashed lines). In **Figure 3a**, the initial TA spectrum of the SM1 blend is very similar to that of the neat film – only differing in the region of stimulated emission (1.5-1.8 eV) – which indicates that singlet excitons are the main excited states present in the BHJ films. The charge-induced absorption becomes visible only after several tens of picoseconds (negative change in transmission at 1.4 eV). An electro-absorption feature around 1.95 eV accompanied the emergence of charges in the SM1 blend and is associated

with those near the interface. In contrast, in SM2 films a charge-induced absorption signature (also just below 1.4 eV) was already present on the sub-picosecond timescale, indicating ultrafast charge transfer. Here, we note that the modest exciton dissociation and charge generation efficiency observed in SM1 blends cannot be attributed to insufficient driving force for charge separation at the heterojunction, because SM1 and SM2 have comparable IP and EA energies.[18] This is confirmed by time-delayed collection field (TDCF) experiments[39] on optimized blends presented in **Figure 3c** and **3d**, which demonstrate that increasing the driving force by applying an external field has virtually no effect on charge generation in the SM1 blends and causes only a limited enhancement in the SM2 blends. Therefore, in the case of SM1 devices, this result indicates that the fill factor of devices is mainly limited by non-geminate recombination competing with charge extraction. However, in the case of SM2, the identical slopes of the TDCF data and the *J-V* data indicate non-geminate recombination is of less importance (except near V_{oc}) and that the device performance becomes limited by (however small) geminate recombination.[40]

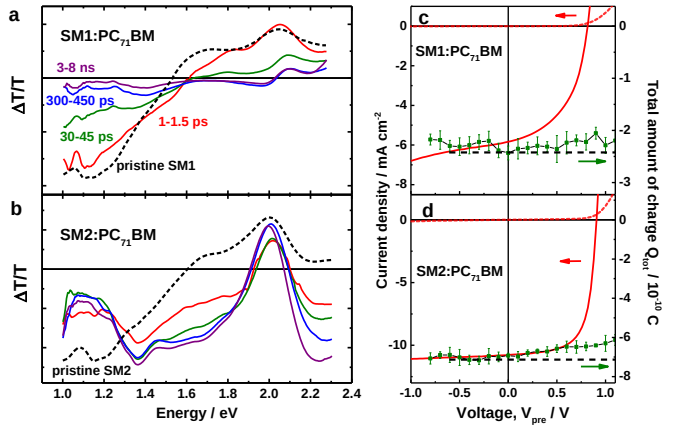

Figure 3. Charge generation in optimized BHJ thin films with SM1 and SM2: (a) Short delay transient absorption (TA) spectra of SM1:$PC_{71}BM$ blends (excitation density 17 μJ/cm^2) and (b) SM2:$PC_{71}BM$ blends (excitation density 1.6 μJ/cm^2). The dashed lines correspond to the spectra of the neat films of SM1 and SM2, averaged from 1 to 1.5 ps (excitation density 4 μJ/cm^2). (c) J-V curves (left axis) and voltage dependence of the total charge Q_{tot} extracted as probed by TDCF experiments (right axis) on an optimized SM1 device and (d) an optimized SM2 device (excitation density for both 0.2 μJ/cm^2). The films were excited with a 100 fs laser pulse at 500 nm for the TDCF experiment and 532 nm for the TA analysis.

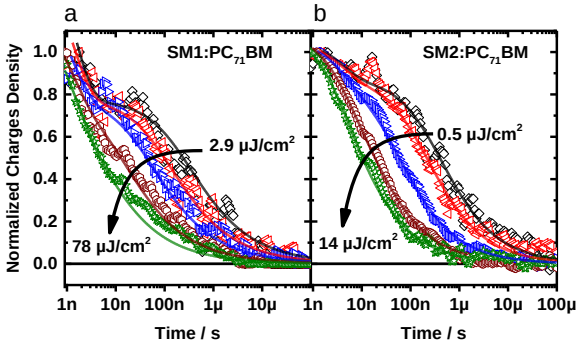

Figure 4. Charge-induced absorption decay dynamics in (a) optimized SM1 blends and (b) optimized SM2 blends (open symbols), and fluence-dependent charge carrier recombination dynamics fitted by a two-pool model (solid lines) (cf. details in the SI). The dynamics were obtained by ns-μs transient absorption spectroscopy. For the SM1:$PC_{71}BM$ blend films, the carrier dynamics were extracted by multivariate curve resolution to the experimental data matrix in order to deconvolute the spectral contributions of excitons, charges, and electroabsorption (cf. detailed methodology in the SI). For SM2:$PC_{71}BM$ blend films, the dynamics were found to be virtually the same across the entire spectral and dynamic range probed (1 ns to 100 μs) and thus were attributed to charges; the dynamics are thus obtained by averaging the decay over the entire photoinduced absorption range (cf. details in the SI).

2.2.3 Charge Carrier Dynamics

Figure 4 shows the fluence-dependent dynamics of the charge-induced absorption between 1 ns and 100 μs as monitored by TA spectroscopy. The recombination channels are inferred from a fit of the experimental data to a two-pool model (see differential equations and analytical solution/fitting expression in the SI). This model assumes that a fraction f of the initial charge carrier population consists of spatially-separated charges, which exhibit a power-law decay with a recombination order of $\lambda + 1 \geq 2$ and a recombination prefactor k_λ. The remaining fraction $1 - f$ of the initial carrier population is attributed to coulombically-bound charges, namely interfacial geminate pairs, which decay according to quasi single exponential dynamics with a time constant τ.[41] The parameters f, λ, k_λ and τ are considered independent of the initial number of charges. Fits to the data for the device-optimized SM1 blends indicate that a fraction $1 - f = 23\%$ of the charges do not undergo charge separation to spatially-separated charges, but recombines geminately instead. This may be related to the presence of the electro-absorption feature in TA measurements, which are caused by charges trapped near the interface (see **Figure 3a** and SI). Indeed, as shown in recent studies,[42–46] the ability of charges to rapidly part from the donor-acceptor heterojunction plays a major role in efficient charge generation. This recombination channel adds to the exciton dissociation losses evidenced earlier for the SM1 devices in the PLQ measurements. Despite the absence of electro-absorption in SM2 blends, our analysis measures a lower, but still finite, fraction of geminate recombination ($1 - f = 13\%$) in these blends.

Turning to the non-geminate recombination channel, the parameters λ and k_λ extracted from the fit enable us to compute the equivalent bimolecular recombination coefficient under one sun illumination (details in the SI).[40] This value allows comparison of the non-geminate recombination rates of systems having different non-geminate recombination orders. Interestingly, the values obtained for SM1 and SM2 are quite similar with (1.6 +/- 0.7) × 10^{-12} and (1.0 +/- 0.2) × 10^{-12} cm^3s^{-1}, respectively. This implies that the difference in fill factor observed in SM1 and SM2 optimized blends (49 and 67%, respectively) is not a consequence of different non-geminate recombination rates, but rather the rate of charge extraction, as discussed in the following section.

2.2.4 Charge Extraction

Although the non-geminate recombination rates are found to be similar in SM1 and SM2 based films, their impact on device performance, more specifically on J_{SC} and FF, can be quite different depending on the dwell time of charges in the active layer prior to charge extraction at the electrodes. To investigate this effect, we first measured J_{SC} as a function of incident light intensity (details in the SI). Prior reports have established that the extent of non-geminate recombination losses in devices can be estimated from the light intensity (I) dependence of the photocurrent described by $J_{sc} \propto I^{\alpha}$.[47] Here, an $\alpha = 1$ indicates negligible non-geminate recombination losses (i.e., most carriers are extracted prior to recombining),[48] whereas $\alpha < 1$ indicates a competition between non-geminate recombination and carrier extraction at *Jsc* conditions. **Figure 5a** and **b** depicts the dependence of J_{SC} on light intensity for the SM1 and SM2-based devices, respectively, cast without and with optimized DIO concentrations. For non-DIO SM1-based active layers, a fit yields α=0.78, indicative of substantial non-geminate recombination losses. In contrast, $\alpha = 0.94$ in optimized SM1 devices, implying significantly reduced recombination losses. Non-geminate recombination can be nearly suppressed upon optimization of the active layer morphology in SM2-based devices where α increases from 0.88 (no DIO) to 0.99 (optimized conditions). Overall, these results are consistent with the figures of merit displayed in **Table 1**.

Transient photocurrent (TPC) measurements provide information on carrier transport and, in particular, on whether carrier traps affect the transport in BHJ active layers.[49,50] TPC experiments have previously been used to investigate the trapping and detrapping rates in a wide range of BHJ devices, including polymer-fullerene,[51–53] "all-polymer",[54,55] and hybrid BHJ solar cells.[50] **Figure 5c-f** depicts the normalized photocurrent transients of cells using long light pulse excitations (200 µs; cf. details in the SI), allowing the current density to reach steady-state conditions. SM1-based active layers show a pronounced dependence on light intensity, with a fast initial rise/fall component followed by a second, slower component (**Figure 5c and 5e**). In the non-optimized SM1 device (no DIO), the fast rise of the current evolves into a transient peak with a slow decay at higher light intensities. A fast/slow decay (1 µs, then 200 µs) is mirrored in the turn-off dynamics. In general, the slower dynamic component becomes less prominent as light intensity increases, suggesting that the traps are filled at higher light intensities and in turn their impact on charge transport becomes less pronounced. In optimized SM1-based active layers, the current does not show any transient peak at high light intensities, and the rise/fall times are up to 10x faster. However, the dual component fast/slow decay dynamics remain. In earlier studies,[54,55] these dynamics have been convincingly described by time-dependent drift-diffusion models, in which the inclusion of trap states reproduced the sequential two-component photocurrent dynamics. Based on those prior reports, we assign the fast component to rapid and efficient transport of free charges, and the slower component to trapping, where trap-mediated space-charge effects are at the origin of the transient photocurrent peak observed at the higher light intensity regime.[9] In optimized SM1-based devices, two factors could account for the disappearance of these transient peaks: a reduction in the depth and density of trap states and/or slower trapping and faster detrapping rates.

Fast, single component dynamics for the SM2-based active layers contrast with those of SM1-based devices and are shown in **Figure 5d and 5f**. The TPC curves of SM2 non-optimized active layers (**Figure 5d**) show only a weak light intensity dependence, with (10%-90%) rise/fall times dropping from 9.5 µs to 4 µs as light intensity increases from 0.11 to 1.43 sun equivalent. Upon device optimization with DIO, the SM2-based device dynamics are virtually independent of light intensity with rise/fall times on the order of 1.8 µs (**Figure 5f**). As DIO concentration is increased beyond optimum to 0.5 v.%, some light-intensity dependence and a weak transient peak are apparent, but it is not as prominent as in the SM1 blend (see **Figure S6**). Single component fast dynamics in the SM2 blend indicates trap-free extraction, and the independence with light intensity in optimized devices, indicates faster transport-limiting recombination. These results are consistent with the power-law (α) analysis of J_{SC} as well as the transient spectroscopy analysis above.

Overall we consistently see the presence of traps in the SM1:$PC_{71}BM$ blend devices slowing extraction and explaining the higher impact of non-geminate recombination losses. However, optimization with DIO enables extraction to compete more favourably with recombination. In contrast, the nearly trap-free carrier transport regime observed in SM2-based BHJ devices is in line with SM2-based photoactive layers outperforming SM1-based devices.

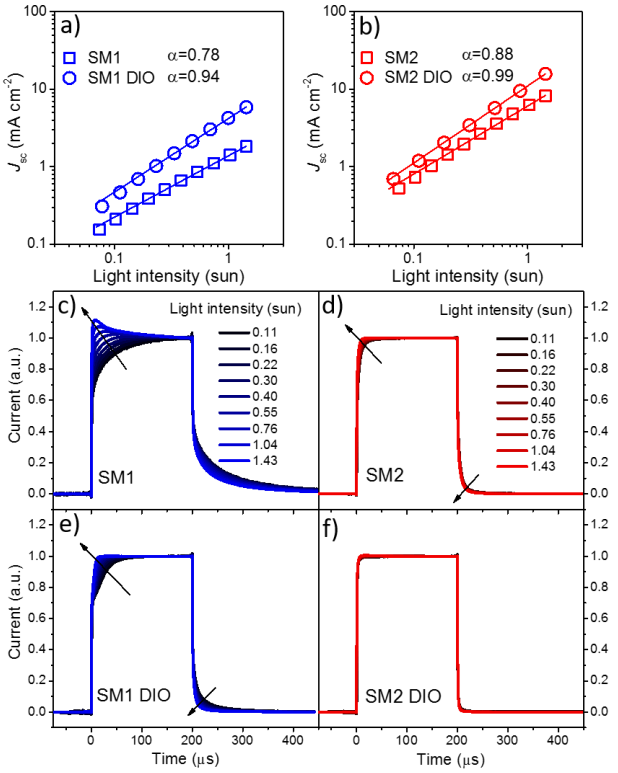

Figure 5. Steady state and transient dependence of J_{SC} on light intensity. (a) Steady state dependence for SM1-based devices without DIO and optimized devices, and (b) the same for SM2-based devices. The solid lines correspond to fits to the data according to $J_{SC} \propto I^{\alpha}$. Intensities are corrected for AM1.5G spectral mismatch. Transient (normalized) response to a 200 µs white light (LED) pulse for (c) non-optimized (no DIO) and (e) optimized (0.5 v.% DIO) SM1-based BHJ devices, and (d) non-optimized (no DIO) and (f) optimized (0.2 v.% DIO) SM2-based BHJ devices. The black arrows emphasize the dependence of the device short-circuit current characteristics as a function of time (after pulse excitation) and light intensities (provided in terms of equivalent sun; cf. details in the SI.

To confirm this interpretation, the *J-V* characteristics of the optimized devices were fitted by an analytical equation for transport limited photocurrents:[56]

$$J(V) = J_G(V)\left\{\exp\left[\frac{eV - eV_{OC}}{(1+a)k_BT}\right] - 1\right\} + \frac{V}{R_{Sh}}$$

Where a is a figure of merit describing the competition between charge generation and extraction according to

$$a^2 = \frac{ek_2d^3J_G}{4\mu_{eff}^2(k_BT)^2}$$

Here, J_G(V) is the (possibly bias dependent) generation current, R_{sh} a shunt resistance, k_2 the non-geminate recombination coefficient, d the active layer thickness, k_BT the thermal energy, and μ_{eff} the effective mobility for charge extraction, which is dominated by the slower carrier.[57,58] Details of the fits are described in the SI. Values for k_2 were taken from the TAS data described above, therefore, the only remaining fit parameter is the effective mobility. The analysis yielded values for μ_{eff} of 1.9×10^{-5} cm^2/Vs and 4.5×10^{-5} cm^2/Vs for the optimized SM1 and SM2, devices, respectively. These values are somewhat higher than our previous space-charge limited current mobility measurements,[18] but are still rather low compared to typical polymer:fullerene blends. They highlight that charge extraction is indeed an issue in these SM:fullerene blends for at least one type of carrier, and that it occurs at a slower rate in the SM1-based blend.

2.3. Structure of the Active Layer

From our spectroscopic measurements thus far, we have found that SM1-based active layers suffer from substantial exciton harvesting limitations (worsened by DIO), whereas exciton harvesting can be considered efficient in SM2-based active layers. We have also shown that SM1-based devices endure slower charge generation, more carrier trapping, and poorer extraction compared to SM2-based BHJ solar cells. Lastly, we have found that the presence of carrier traps increases recombination losses in SM1-based devices. To investigate the structural origins of those distinct patterns of exciton and carrier dynamics, we now turn to a combination of X-ray and Neutron scattering and microscopy techniques well suited to the study of these materials. In particular, in the following sections, we characterize both the lateral and vertical domain morphologies, as well as the molecular packing and crystallinity across the active layers.

2.3.1 Lateral Morphology

In **Figure 6**, we provide lateral composition maps from scanning transmission X-ray microscopy (STXM) experiments. Details of this analysis are presented in the SI, which involved previously reported procedures.[32,59] Similar to our previous bright-field TEM measurements,[18] we find that SM1 blends have large (~100 nm) phase-separated domains, while domains are not discernable in either SM2 blend. Our STXM analysis additionally indicates a web-like domain structure rich in SM1 when cast from neat CB transforming to a more disconnected structure of SM1-rich islands when DIO is added to the solution. Here, the SM1-rich islands that form are more obvious than in our previously reported TEM analyses. In addition to this general domain structure, quantitative analysis reveals that the SM1-rich islands are pure (possibly with a thin fullerene shell caused by surface energy differences). The composition of the islands integrated through the film thickness is 98±4% SM1 while the fullerene-rich surrounding matrix is 15±5% SM1 (see **Figure 6b** and Section S8 in the SI). The compositions of domains cast from neat CB were too small to quantify with STXM, but the scattering measurements below indicate that the domains are at least as pure – possibly more so.

We also performed polarized STXM experiments to track the liquid-crystalline ordering of the films as revealed in our previous work.[18] Figure S12 demonstrates liquid crystalline alignment in neat films of both SM1 and SM2 over length-scales of 500 nm to a few microns. Furthermore, this alignment is preserved in each of the

SM1 blends on length-scales similar to pure films, encompassing several 100 nm domains. Such ordering would likely aid charge transport between domains if there was a significant concentration of the molecules in both phases.

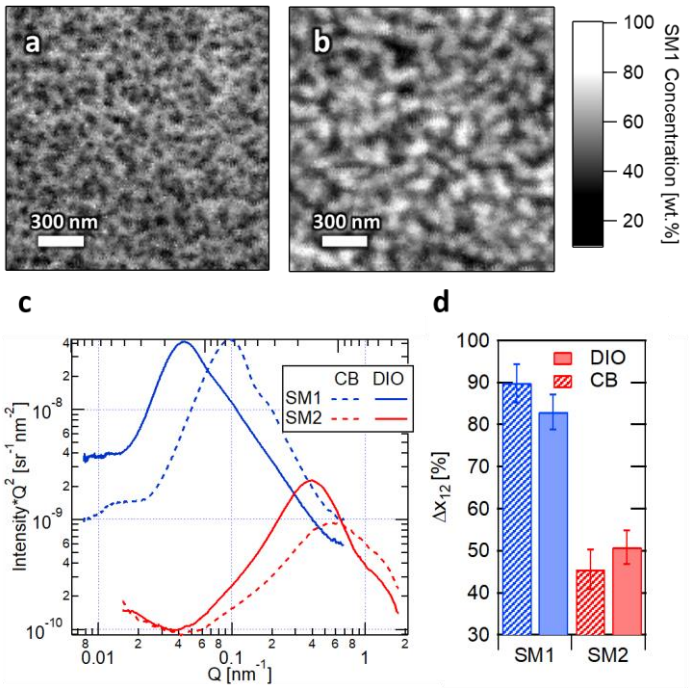

Figure 6. Investigation of the lateral morphology. STXM composition maps of SM1:$PC_{71}BM$ OPV active layers cast a) without and b) with the DIO solvent additive (optimized conditions). Colors have been scaled based on quantitative composition analysis detailed in the SI. c) Lorentz corrected RSoXS scattering profiles at 283.5eV. "CB" indicates devices cast from CB-only, while "DIO" indicates devices cast from optimized DIO concentrations. d) Composition difference Δx_{12} (of the SM) between domains 1 and 2 in a two-domain model based on combined analysis of STXM and total scattering intensity from RSoXS. (See SI for details of the analysis.)

Since devices cast on MoO_x surfaces performed better than those cast on PEDOT:PSS for the anode, we compared STXM images of the lateral morphology of the SM1 active layers on each surface (Figure S10). The results show no significant difference. Thus the lower performance on PEDOT:PSS could be from the acidic protonation of the pyridyl nitrogen of the PP motif similar to what was found for the p-DTS$(PTTh_2)_2$ molecule.[20]

STXM experiments were complemented by resonant soft X-ray scattering (RSoXS) on separate pieces of the same films as exhibited in **Figure 6c** (see Experimental Section for sample preparation details). For the SM1 blends, scattering peaks were observed at $Q = 0.0977\ nm^{-1}$, when cast from neat CB, and $Q = 0.0440\ nm^{-1}$ with optimized DIO, corresponding to characteristic domain-domain spacing ($l=2\pi/Q$) of $l_{CB1} = 64\ nm$ and $l_{DIO1} = 143\ nm$, respectively, where subscripts label solvent (CB or DIO) and the SM (1 or 2). This is in good agreement with the domain spacing seen in the STXM images, with the domain sizes themselves being somewhat smaller than the spacing but both significantly larger than estimates the of exciton diffusion length (~10nm). RSoXS profiles of SM2 blends reveal domains as well, despite the lack of evidence from either STXM or TEM imaging. The characteristic lengths (domain spacing) are $l_{CB2} = 12\ nm$ and $l_{DIO2} = 16\ nm$ – within range of exciton diffusion lengths. We note that the RSoXS profiles have not been fit to formal models and, therefore, the characteristic lengths quoted are provided as estimates. Domain sizes on the order of these lengths are below the resolution of STXM. Additionally, these length scales are well below that of the film thickness, suggesting that there likely exists 3D structures that would obfuscate results of transmission microscopies, which is not an issue for scattering. Thus domains appear to be present in all samples despite our inability to discern them via electron or X-ray microscopies. In a similar analysis to our previous work,[60] Figure S15 shows RSoXS evidence of SM1 orientational domains in blends consistent with polarized STXM. Remarkably, while there is little sign of alignment in SM2 blends cast without DIO, scattering signals of molecular alignment do emerge in optimized SM2 blends, correlating with increased aggregation measured in absorbance spectroscopy and suggesting a similar inter-domain molecular alignment seen for SM1 blends.

Compositional domain interfaces can also be probed by the power-law dependence of scattering intensity at high-Q. Interestingly, the $I(Q)$ plots reveal that the SM1 samples follow a q^{-p} intensity fall-off with $p \cong 4$, indicating sharp and smooth interfaces. Diffuse interfaces cause faster fall off (e.g., $p{\sim}5$), while rough/fractal interfaces cause slower fall-off (e.g., $p{\sim}3$).[61] Specifically, fits result in $p_{CB1} = 4.2 \pm 0.1$ and $p_{DIO1} = 3.8 \pm 0.1$ while the data does not extend far enough for the SM2 blends to be analyzed quantitatively (see Figure S16). Sharp and smooth interfaces is different from fractal interfaces exhibited in P3HT:PCBM systems.[62] However, the lack of polydisperse polymer chains in SM-fullerene BHJs may result in sharper crystal boundaries.

The STXM measurement of absolute domain purity on the SM1 (0.5 v.% DIO) blend film scales the RSoXS total scattering intensity (TSI), enabling us to calculate composition fluctuations in each film based on a two-phase model. The results are shown in **Figure 6d** (see Section S12 in the SI for details of the analysis). As discussed above, the domains are very pure in both SM1-blend films with the impure domain containing only 10-15 wt.% of the minor component (predominately SM1 within fullerene-rich domains). While this may not be detrimental in polymer-fullerene systems where polymer tie-chains between crystallites enable percolation of charges even down to < 5 wt.% concentrations,[63] such compositions are at or below the percolation threshold for particles in three dimensions (between 12-18 v.%).[64] In contrast to what is found in the SM1-blends, the calculated domain composition variation for the SM2-blends is considerably lower at $\Delta x_{CB2} = 46 \pm 5\%$ and $\Delta x_{DIO2} = 51 \pm 4\%$. In this model, if one phase is pure, then Δx is the composition

of the other phase. However, on the sole basis of this level of analysis, another assumption could be that neither phase is pure. Either way, domains are such that their composition sets them above the percolation threshold for charges in the minor component, explaining the reduced carrier trapping processes observed earlier by TA and TPC in SM2 blends compared to SM1.

2.3.2 Vertical composition profiles

Neutron reflectometry (NR) was performed on the neat and the optimized 1:1 (w/w) blend films for both SM1 and SM2 to assess the vertical phase composition profiles that might affect device performance.[91] First, the scattering length densities (SLDs) of the neat SM films spin-coated onto silicon wafers from chlorobenzene were determined (Figure S17a and b). The SMs were found to have the same mass density of 1.19 g cm^{-3} in the thin films, resulting in SLDs significantly lower than that of $PC_{71}BM$[65] and, therefore, selective deuteration was not required in the blend films (see Table S3 for all modelled SLD values). Inclusion of DIO in the spin-coating solution resulted in a similar bulk SLD in both neat SM1 and SM2 films. However, significant roughening of the SM1 film at the air interface became apparent – consistent with the observed crystallization. In the case of the neat SM2 film, only minor roughening occurred when DIO was added. We next measured the blend films deposited onto MoO_x coated silicon wafers to reproduce the device architecture with results in Figures S17c and S17d. The SM2:$PC_{71}BM$ film reflectivity profile could be modeled with two layers with the bulk layer corresponding to an SM2:fullerene weight ratio of 1:(0.93 ± 0.15). At the air interface, there was a $PC_{71}BM$-rich layer, (Figure S17d) corresponding to 1:(1.66 ± 0.30). The increase in $PC_{71}BM$ concentration at the top surface should enhance electron extraction at the cathode. The largely uniform vertical profile in the bulk of the SM2 blend film is consistent with the mixed domains that are present in the STXM and TEM data.

In contrast, the SM1 blend system revealed a highly non-uniform depth profile, which could only be successfully modelled using discrete density profiling (DDP, see details in the SI). Here the higher SLD fullerene accumulated in the middle of the active layer. Importantly, the average SLD across the layer corresponds to an SM1:fullerene weight ratio of 1:(0.96 ± 0.16) – in agreement with that of the processing solution. Lower SLD values were observed at the air and substrate interfaces compared to the middle of the film. At the air interface the SLD value (below that of SM1) indicates a rough surface – likely a consequence of the large crystalline domains in the film. The dip in SLD at the blend/MoO_x interface suggests a nonuniform and/or SM1-rich interface. Furthermore, the SLD of the MoO_x film was lower than that in the SM2 blend sample, consistent with the absorption of atmospheric moisture.[66] The presence of voids at a nonuniform film/MoO_x interface would allow ingress of such moisture. Overall, the heterogeneous profile in the SM1 blend film is in agreement with the large size and relatively pure domains revealed in the analysis of the lateral morphology and could result in regions of charge trapping, poorer charge extraction, and other losses discussed earlier.

2.3.3 Crystallinity

Grazing incidence wide angle X-ray scattering (GIWAXS) experiments were performed to characterize the crystallinity of SM1 and SM2. Results of the experiments are shown in **Figure 7**, and additional results and discussion are provided in the SI. Neat films without DIO (**Figure 7a** and **7b**) of both SMs were aggregated but weakly (long range) ordered. The peaks at Q ~ 4 nm^{-1} and 17 nm^{-1} can be attributed to intermolecular distances along the alkyl sidechain direction and the π-π stacking direction respectively. In neat SM1, the π-π stacking peak is preferentially oriented in the in-plane direction, indicating an edge-on orientation. In contrast, the out-of-plane π-π stacking peak in neat SM2 indicates a preferred face-on orientation. in addition, there is an isotropic component to the scattering peaks in films of both neat SMs.

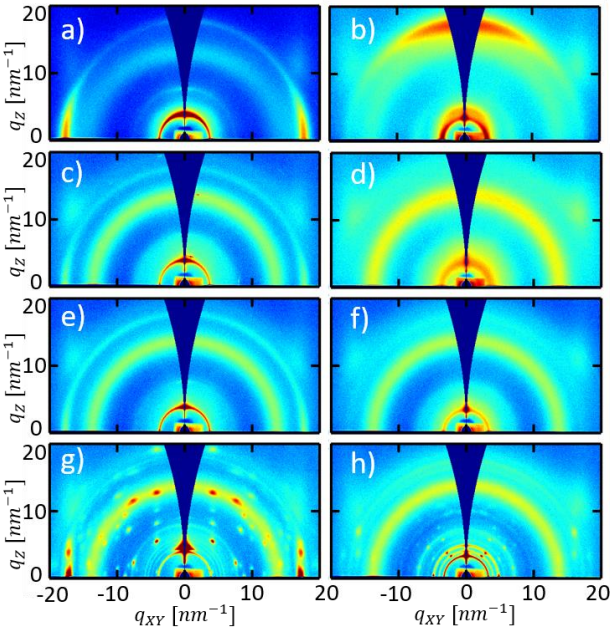

Figure 7. GIWAXS scattering results. a) & b) are neat films of SM1 and SM2, respectively, cast without (0 v.%) DIO (CB only). c) & d) are from corresponding blend films cast from 0 v.% DIO; e) & f) are blend films cast from 0.2 v.% DIO; and g) & h) are blend films cast from 0.5 v.% DIO. Si substrate is responsible for broad peak at approximately $(Q_{XY}, Q_Z) = (16.4, 10.7) nm^{-1}$. All images are corrected for Monitor and film thickness and displayed on the same logarithmic color scale.

In blend films with no DIO (**Figure 7c** & **7d**), SM1 shows a sharp alkyl stacking peak, again with preferential edge-on orientation, whereas the SM2 scattering is broad and isotropic, indicating higher disorder and perhaps some intermixing of SM2 compared to SM1 in the blend. Additionally, the π-π stacking peak was better defined in the SM1 blend compared with SM2, where it was barely discernable. Increasing the DIO concentration from 0 to 0.2 v.% (**Figure 7e** & **7f**) had no significant effect on the

SM1 blend but decreased the width of the alkyl stacking peak in the SM2 blend, indicating an increase in order while the orientation distribution remained isotropic. Despite this, the overall degree of order remained low in both blends with few detectable peaks. Further increasing the DIO concentration to 0.5 v.% (**Figure 7g** and **7h**) changed both SM blends from films with merely stacked aggregates to films with well-defined 3D crystals, giving rise to resolvable Bragg peaks. A full structural characterization of these molecules is outside the scope of this work but will be presented in a future publication. Interestingly, the preferential edge-on orientation of SM1 could contribute to the lower μ_{eff} measured in our *J-V* analyses discussed in earlier sections.

A Scherrer analysis was used to estimate the aggregate coherence length from the widths of the scattering peaks. This analysis mainly provides a lower limit to the coherence length, since both instrument resolution (calculated as $\Delta q \sim 0.3/nm$ or $40\,nm$ max) and paracrystalline disorder also contributes to peak width.[67,68] In our analysis, we focused on the peaks at the smallest Q in the data presented here (the lamellar stacking peaks). The neat and blend SM1 films with 0-0.5 v.% DIO had peak widths that are at the resolution limit, pointing to coherence lengths >40 nm. This means that aggregate sizes must also be >40 nm in at least one dimension as coherence requires a continuous aggregate. The coherence length of the SM2 neat film was 20 nm, and the blend films had coherence lengths of 9, 17, and >40 nm for 0, 0.2, and 0.5 v.% DIO additive, respectively. These aggregate sizes are approximately consistent with domain spacing measured via RSoXS.

It is notable that the crystalline order of SM2 remained low with 0.2 v.% DIO (the optimized amount) and only becomes significant at higher DIO levels. Also, the degree of crystallinity of the small molecule in the optimized film of SM1 is significantly higher than in the optimized film of SM2. Here, our in-depth morphological analyses provide a more detailed description of the aggregation patterns in actual blends with SM1 and SM2 than that discussed in our earlier work.[18] We attribute the apparent switch in ordering behavior measured here to the fact that optimum concentrations of DIO can crystallize SM1, but leaves SM2 relatively disordered. In general, the rise in crystalline order with DIO is consistent with absorbance spectroscopy (**Figure 1d**), from which a large change in aggregation is measured between 0.2 and 0.5 v.% DIO. The increase in aggregation from 0 to 0.2 v.% DIO in the SM2 blend is similarly reflected in the diffraction data and is likely an important aspect of the increased device performance.

3. Discussion

3.1. Nanoscale morphology and its origin

When combining the structural measurements, a clear picture emerges in terms of domain size, ordering and composition across the active layer. First, the SM1 blends are composed of pure phases of SM1 aggregates as demonstrated by the STXM analysis. These domains grow from ~50 nm in lateral diameter to over 100 nm when DIO is added to the processing solvent (as seen in STXM and RSoXS) and SM1 crystallizes (as shown by GIWAXS). In both cases, these aggregates are surrounded by a nearly pure (85-90 wt.%) matrix phase of fullerene as indicated by the TSI analysis. In contrast, the SM2 blends are composed of much smaller (~10 nm) domains – again coarsening with DIO as revealed by the RSoXS profiles. At least one of the domains is more mixed (from the quantitative TSI analysis, **Figure 6d**), with the RMS composition fluctuation only $\Delta x = 46 - 51\ wt.\%$. The quantitative similarity of the characteristic lengths measured in RSoXS to the coherence length calculated from Scherrer analysis of the GIWAXS data reveals, however, that the SM2-rich phase is actually composed of some pure SM2 aggregates, and thus the "fullerene-rich" phase can hardly be considered 'rich' as it is about $46 - 51\ wt.\%$ fullerene. This is under the assumption of a two-phase model; although, here we note that there are pure fullerene regions present in the active layer in light of the fullerene scattering halo seen in GIWAXS.[17,69]

With compositions of the phases approximately known, we also know the domain volume fractions from the TSI analysis. From this analysis, Figure S14b (left-most points on red traces) indicates that the pure SM2 aggregates are the minority phase by volume - only 15-20 v.%, making it likely that this phase is in fact relatively discontinuous, i.e., the domains are not strongly interconnected. Thus a majority of the SM is actually in the mixed phase. By contrast, the phase volume fractions recently estimated in another SM system are more balanced at 50-50 v.% making domain continuity more likely.[17] In that study, fairly pure phases likely benefitted from increased connectivity. The phases in the SM1 blends also have a more balanced (equal) volume ratio, in agreement with STXM, although with DIO additive in the processing solvent, the pure SM1 phase is nodular and disconnected, demonstrating that balanced volume fractions can still result in discontinuous phases. Possibly of critical importance is that the remaining SMs (1 or 2) in the mixed (fullerene-rich) phase appear to align with each other as is demonstrated by both the polarized STXM (Figure S12) and RSoXS (Figure S15) analyses. Such ordering can only result from intermolecular interactions between the minority SMs within the fullerene-rich matrix, and could lead to electronic interaction, connecting SM aggregate domains. Putting all of these results together, we schematically picture the nanoscale morphology of the two blends in **Figure 8** with the main difference being the composition of the SM in the matrix phase.

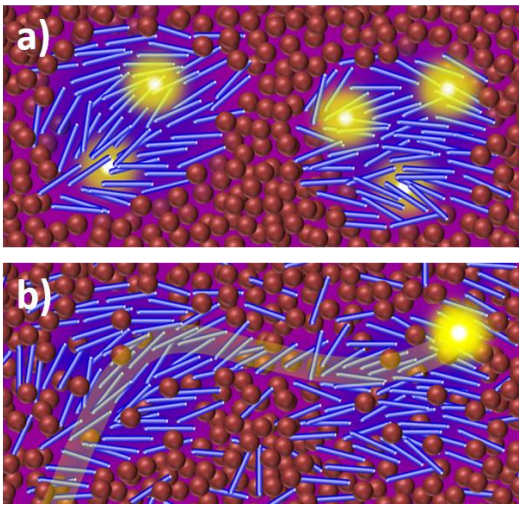

Figure 8. Schematic representation of the SM1 and SM2 blend morphologies with the SM donors (blue), fullerene acceptor (red), and charges forming in those blends (yellow). a) Isolated pure domains limit interfacial area and trap charges (SM1 blends with domains depicted smaller than reality to highlight molecular isolation), whereas b) mixed domains (SM2 blends) maximize charge generation and enable percolating pathways for charge transport.

From this analysis, we further conclude that the DIO solvent additive primarily acts as a plasticizer to enable ripening of the domains, aggregation of the molecules, and eventually ordering of large crystals. Domain evolution and crystallization have been reported for the small molecule system *p*-DTS(FBTTh$_2$)$_2$:PC$_{71}$BM,[30,38] but one important difference with the reported and current work is that for the *p*-DTS(FBTTh$_2$)$_2$ the domains became purer with added DIO, whereas in our systems the domain composition was fairly invariant with the DIO concentrations that were investigated as indicated by the TSI measurement. This composition invariance is similar to the behaviour we reported for the polymer-fullerene PTB7:PC$_{71}$BM system[32] (same BDT moiety as the SMs studied here) where the domain compositions were measured to be the same as thermodynamic equilibrium compositions regardless of the DIO content. Thus the systems studied here appear to also be at compositional equilibrium. Due to the different levels of mixing we have measured, it is apparent that the SM-fullerene miscibility is higher for SM2 blends than for SM1 blends.

3.2. Structure governing device dynamics

Our DIO concentration-dependence study reveals a threshold for "high crystallinity" which significantly affects all stages of charge generation – but particularly exciton dissociation. For both systems, the SM donor crystallizes after 0.5 v.% DIO after exhibiting only local aggregate packing. For the SM1 system, what starts out as detrimentally large domains with respect to the exciton diffusion length is exacerbated by domain ripening caused by the presence of DIO (known to stay in the film for hours). This leads to poor exciton harvesting efficiency (<50%) with DIO as evidenced by the increasing exciton PL signal, long exciton lifetimes in the PL transients, and delayed charge generation evidenced by the TA measurements. The small, mixed domains in the SM2 system, by contrast, expand only slightly with addition of 0.2 v.% DIO (optimal conditions), preserving the interfacial exciton harvesting and ultrafast charge generation. Large-scale SM2 crystallization induced by increasing the DIO concentration to 0.5 v.%, suppresses exciton harvesting (PLQ ~88%, **Table 1**) likely due to the larger pure crystallite/domain size (>40 nm).

The large and pure domains of SM1 further limit connectivity for charge transport. Indeed space-charge build-up measured via TPC for the SM1 devices goes hand-in-hand with the pure disconnected SM1 domains resulting in large populations of bound geminate pairs and charges trapped in domain islands. Charge recombination is particularly high in SM1 devices without DIO due to the low ordering. With the onset of crystallinity from DIO, improved charge generation and extraction prevails over the extra excitonic losses in devices, explaining the concurrent rises in J_{SC} and V_{OC}. In fact, at short-circuit, current densities are well accounted for simply by considering the donor band gap, PLQ, and geminate recombination measured in TA spectroscopy. However, even when optimized, non-geminate losses from trapping continue to play a significant role in the SM1 system as evidenced by sub-linear J_{SC} ($\alpha < 1$), two-component TPC dynamics, and electroabsorption features in TA spectroscopy (perhaps from the sharp interfaces measured with RSoXS where local fields from neighbouring geminate charges are aligned). Consequently, charge extraction is slowed, increasing recombination likely at domain boundaries or isolated SM molecules within fullerene-rich domains. This reduces device fill factors compared with the SM2 system, in spite of SM2 having lower crystallinity and higher mixing propensity. TDCF charge extraction remains low in the optimized SM1 device, consistent with charges being spatially trapped in domain islands (**Figure 8** top), and is likely a main cause for the difference in performance between the material systems.

The contrasting morphologies of the SM1 and SM2 blends correlate with equally contrasting device dynamics and performance. Mixing within domains, although beneficial for exciton harvesting, has been linked to increased charge recombination (geminate or non-geminate),[32] with several polymer-fullerene BHJ solar cell studies identifying high domain purity as important to maintain low recombination rates by separating charges into spatially-segregated domains.[14,15] Thus, our analysis of the SM2:PC$_{71}$BM devices (with the mixed domains) indicates that ca. 13% geminate recombination occur in optimized devices –a recombination channel expected to limit internal quantum efficiency to some extent. Meanwhile, non-geminate losses in SM2 blends are quite low –an interesting observation considering that the measured bimolecular recombination rates are similar in SM1 and SM2 blends (while the carrier mobilities in

optimized SM2 blends remain fairly modest). Total non-geminate losses in BHJ solar cells are, however, determined by a competition between recombination and extraction. Direct, trap-free charge percolation routes through mixed phases is the likely reason for the low non-geminate losses observed in the SM2 blends. Here, we note that 50% mixing in domains is well above the 3D charge percolation threshold,[64] and the molecular alignment in the matrix phase, furthermore, may be promoting pathways of aggregates and, in turn, efficient charge transport to the electrodes (**Figure 8** bottom).[69,70] This would explain the absence of charge trapping and linear relationship for the J_{SC} ($\alpha \cong 1$) with light intensity.

It should also be noted that, from our analyses, sufficient charge generation and transport occurs in the SM2 blends when crystallinity remains relatively low. This is all the more interesting, since device performance improves significantly with SM1 blends when SM1 crystallizes. Increased molecular ordering aids in charge transport in both systems, but the ordering measured in optimized SM2 is local molecular alignment (aggregation) rather than the long range ordering (crystallinity) measured in the optimized SM1 blend. While inducing crystallinity in SM2 blends could in principle enhance performance further by lowering non-radiative energy losses across the active layers,[71] the lack of control over crystal size at the time of solution processing remains a key limitation.

Overall, the BHJ device efficiencies of 6.5% obtained with SM2 are convincingly high given that (i) SM2 is a wide optical-gap material (1.87 eV) and (ii) active layers cast with SM2 must remain relatively thin (90 nm; thus not fully absorbing above-gap photons). In comparison, P3HT:$PC_{61}BM$ devices can be made optically thick with the same optical gap, but perform more modestly, mainly because of the larger V_{OC} losses. We also note that the efficiencies of 6.5% are in line with those reported earlier in $DTS(BTTh_2)_2$-based BHJ solar cells, while $DTS(BTTh_2)_2$ is a narrower-optical gap material for which a higher J_{SC} can be obtained, albeit with a lower V_{OC}.[20]

As stated earlier, optimized devices made with SM2 benefit from suppressed exciton recombination and exhibit only little non-geminate recombination. However, if geminate recombination (13%) could be eliminated in SM2 blends, device efficiencies would increase to ca. 7.5%. Engineering the local molecular orientation and crystallinity at interfaces are likely pathways to such an improvement – a possibility given the low-ordered state of the donor material in the corresponding 'optimized' BHJ solar cells. Such increased ordering would likely translate into an increase in charge mobility across the active layer (currently approx. one order of magnitude below record setting devices),[8] leading to higher fill factors in optically thick films. Thicker films would further increase photocurrents to line up with record-setting SM devices at 10% efficiency.[8] Substituting SM2 with fluorine substituents could further deepen its HOMO, while inducing a better band alignment with $PC_{71}BM$, and increasing the *V*oc of the BHJ solar cells to a significant extent. Those propositions are consistent with predictions that even wide-bandgap devices could achieve >13% efficiencies and $V_{OC} > 1V$[2] (SM2-based devices already achieve 0.95V).[2] With such improvements, these cells would be ideal high-bandgap subcell materials in a tandem device or used in semitransparent applications such as window laminates.[23]

3.3. Guidelines for SM-OPV nanostructure

Turning to the design and examination of small-molecule systems with gradually improving efficiencies, several trends are emerging. In general, the low amounts of plasticizing DIO (<1 v.%) additive required for the optimization of the best devices points to the fact that such molecules are in general easier to crystallize than polymers, but lack the self-limiting crystal size inherent to polymers, which arises from chain folding.[72–74] Thus, large (>>10nm) crystal sizes are a more common morphological limitation that impacts charge generation. To achieve small, highly crystalline domains, processing methods to kinetically trap small, highly ordered crystallites need to be identified.

Equally important is our clear finding that charge trapping occurs within high-purity, disconnected domains while the mixed-phase system performs well, with limited carrier recombination. This observation implies that, in SM donor-fullerene systems, high-domain purity is not a requirement for device efficiency, in contrast to the arguments made from the examination of polymer-fullerene BHJ solar cells in earlier work.[13–15] In polymer-fullerene BHJ devices, charge trapping in pure polymer domains is not an issue, because polymer entanglements (*e.g.* tie-chains between crystallites) enable connectivity for charges throughout the active layer even down to polymer compositions of a few volume percent.[63] Rather, pure polymer domains are necessary to induce adequate aggregate packing. In contrast, our results show that SM systems can pack even within small or mixed domains. We thus propose that in some SM systems, a possible target goal would be high miscibility to ensure mixed phases that promote charge percolation through the minority component, but maintain the ability of the majority component to aggregate. **Figure 8** illustrates this concept of charge percolation through a mixed, yet ordered, matrix. One apparent route to achieve such morphologies is to include ring-substituents in SM side chains (as in SM2), which seemingly results in an increase in SM miscibility with $PC_{71}BM$ (as seen in the present study). Our result provides impetus for further measurements on other SM donor-fullerene blends to probe the generality of these morphology guidelines to maximize performance.

4. Conclusions:

In summary, we have investigated the steps in the photocurrent generation and extraction processes of a

high-performing, wide optical-gap SM donor-fullerene BHJ solar cell and correlated these results to an in-depth study of the morphology of the active layers used in devices. We found that the processing additive DIO primarily acts as a plasticiser that increases the size of phase-separated domains, as well as the alignment and aggregation of the SM donors and fullerene acceptor across the active layers. As DIO concentrations are increased over a threshold between 0.2 and 0.5 v.%, local ordering gives way to large scale crystallization, which – while aiding charge transport– also severely reduces exciton harvesting, ultrafast charge generation, and connectivity for charge extraction. Prior to crystallization, the morphology appears to arrive at a compositional equilibrium where in one system (SM1) a low miscibility results in large pure phases, while the higher miscibility of the other (SM2) yields smaller mixed-phase domains. While pure phases are found to hinder charge generation and increase charge trapping, the mixed-phase system exhibits excellent charge generation and transport, likely due to greater interfacial area and more favourable pathways for charge migration through the mixed domains. Our findings point to the idea that mixed phase SM systems (i.e., systems with high miscibility) could be a target for high efficiency in contrast with polymer-fullerene BHJ solar cells, where the presence pure domains is important. This goal can be realized through a mitigation of the packing propensity of the SM systems via –for example here– the incorporation of (non-coplanar) ring-substituents in places along the SM backbone, which facilitates the miscibility with fullerenes (at the expense of SM crystallization). If confirmed, this design principle could be exploited in a more systematic manner in the design of high-efficiency SM OPVs.

5. Experimental Section

The materials synthesis was reported in our previous publication as was device fabrication methods and testing.[18] Further details specific to this work are described in the SI.

For time-resolved photoluminescence (TRPL) spectroscopy and transient absorption spectroscopy (TAS) measurements, thin films were spin-coated on quartz substrates using the same protocol as used for the active layer of optimized solar cells. For the TRPL in solution we used a concentration of 10^{-4} mol/L in chlorobenzene. TRPL spectra were recorded using a Hamamatsu streak camera C4742 system equipped with a synchroscan unit. Samples were excited with 100 fs pulses at 80 MHz repetition rate provided by a titanium: sapphire laser (Coherent Vitesse), frequency doubled with a β-Barium Borate crystal, resulting in an excitation wavelength of 400 nm. TAS measurements were performed with a home-built pump-probe setup. Two different configurations of the setup were used for either short delay, namely 100 fs to 8 ns experiments, or long delay, namely 1 ns to 100 μs delays. Further details of this experiment can be found in the Supporting Information.

For time-delayed collection field (TDCF) measurements, devices were prepared according to the protocol described above. For photoexcitation we used the output of a titanium:sapphire femtosecond amplifier (Coherent LIBRA HE, 3.5 mJ, 1 kHz, 100 fs) coupled to an optical parametric amplifier (Coherent OPerA Solo) to generate 500 nm pulses of 100 fs pulse length. Field-dependent generation measurements were performed by applying a prebias pulse (Agilent 81150A) during excitation whose amplitude was varied from -0.8 to 1.1V. An extraction voltage of -2V was applied 5 ns after the excitation laser pulse using the same pulse generator (Agilent 81150A). The resulting current was pre-amplified in a homemade preamplifier circuit integrated in the sample holder and then measured with an Agilent DSO9054H oscilloscope via a 5 Ω input resistor. The total photogenerated charge Q_{tot} was obtained by integration of the current transient up to 500 ns. A small diode area (1 mm²) was used in order to reduce the RC-response time of the entire measurement circuit.

The light intensity measurements were performed with PAIOS instrumentation (Fluxim). The light source is a white LED with 200 mW cm^{-2} of maximum light intensity. In accounting for spectral mismatch, 70% of the maximum irradiance of the white-light LED was used to reproduce the J_{SC} values normally achieved under standard AM1.5G solar illumination (100 mW/cm^2) and represent 1 sun equivalent.

TPC analyses provided the time-dependent extraction of photogenerated charge carriers. During the measurement, the device was set under short-circuit condition; a 200 μs light pulse was used allowing the current density to reach the steady-state condition. The devices were otherwise kept in the dark between pulses in order to avoid any influence of pulse frequency on the current responses.

STXM and NEXAFS measurements were performed at the Advanced Light Source (ALS) bending magnet beamline 5.3.2.2.[75] The setup of the instrument, acquisition protocols, and processing methods were identical to those reported elsewhere.[59] Samples were prepared by the KAUST researcher who processed the devices to assure the same morphology. The films cast on both PEDOT:PSS and MoOx were freed from their substrate by floating on water. Freed films were picked up by Cu TEM grids (no support, Gilder).

RSoXS was conducted at the ALS beamline 11.0.1.2 which uses an elliptically polarized undulator source. Instrument setup, acquisition protocols, and processing methods were identical to those reported elsewhere.[76,77] Separate fragments of the same films used in STXM measurements, once freed from their substrates, were picked up by 100 nm thick SiN membranes (2x2mm lateral size, Norcada).

GIWAXS was acquired at beamline 11-3 at the Stanford Synchrotron Radiation Lightsource at SLAC with an incident angle of 0.2°, and energy of 12.7 keV, a sample-detector distance of 250 mm, and 5x60-second exposures which were averaged. Further details of the sample preparation and data analysis can be found in the Supporting Information.

NR measurements were performed using the Platypus time-of-flight neutron reflectometer and a cold neutron spectrum (0.28 nm < λ < 1.80 nm) at the OPAL 20 MW research reactor [Australian Nuclear Science and Technology Organisation (ANSTO), Sydney, Australia].[78] 24 Hz neutron pulses were generated using a disc chopper system (EADS Astrium GmbH) in the medium resolution mode ($\Delta Q/Q$ = 4.5%) and recorded on a two-dimensional helium-3 neutron detector (Denex GmbH). Reflected beam spectra were collected at incidence angles (θ) of 0.65° for 1800 s and 2.50° for 7200 s to give a range of momentum transfer Q of 0.08-1.96 nm^{-1} [$Q = (4\pi/\lambda)\sin\theta$]. Direct beam measurements were collected under the same collimation conditions for both reflection angles for normalisation. Experiments were conducted in a custom-built sample chamber

under a coarse vacuum. NR analysis procedures can be found in the supporting information.

Supporting Information
Supporting Information is available from the Wiley Online Library or from the author.

Acknowledgements: The authors declare no competing financial interest. O. Alqahtani was supported by Prince Sattam bin Abdulaziz University in Saudi Arabia and the Saudi Arabian Cultural Mission in the US. T. Ferron was supported by the Washington State University Seed Grant Program. A.P and D.N. acknowledge financial support from the German Ministry of Science and Education (project UNVEIL). V.S. acknowledges financial support from the NDSEG fellowship. This research used resources described above of the Advanced Light Source, which is a DOE Office of Science User Facility under contract no. DE-AC02-05CH11231 and Stanford Synchrotron Radiation Lightsource. P. M. Beaujuge acknowledges support by the King Abdullah University of Science and Technology (KAUST) Office of Sponsored Research (OSR) under Award No. CRG_R2_13_BEAU_KAUST_1 and under KAUST Baseline Research Funding. The authors also wish to acknowledge the Australian Centre for Neutron Scattering (formerly the Bragg Institute at the time of the measurements) and the Australian Nuclear Science and Technology Organisation (ANSTO) for providing the neutron research facilities for the NR experiments. The NR measurements were supported by an Australian Research Council Discovery Program (PD120101372). The authors would like to thank Dr Andrew Nelson, Dr Ravi Chandra Raju Nagiri and Mr Jake McEwan for their assistance in performing the NR measurements.

Received: ((will be filled in by the editorial staff))
Revised: ((will be filled in by the editorial staff))
Published online: ((will be filled in by the editorial staff))

References

[1] W. Zhao, S. Li, H. Yao, S. Zhang, Y. Zhang, B. Yang, J. Hou, **2017**, DOI 10.1021/jacs.7b02677.
[2] D. Baran, T. Kirchartz, S. Wheeler, S. Dimitrov, M. Abdelsamie, J. Gorman, R. Ashraf, S. Holliday, A. Wadsworth, N. Gasparini, P. Kaienburg, H. Yan, A. Amassian, C. J. Brabec, J. Durrant, I. McCulloch, *Energy Environ. Sci.* **2016**, *9*, 3783.
[3] R. A. Janssen, J. Nelson, *Adv. Mater.* **2013**, *25*, 1847.
[4] L. J. A. Koster, S. E. Shaheen, J. C. Hummelen, *Adv. Energy Mater.* **2012**, *2*, 1246.
[5] B. W. D'Andrade, S. R. Forrest, *Adv. Mater.* **2004**, *16*, 1585.
[6] N. C. Giebink, G. P. Wiederrecht, M. R. Wasielewski, S. R. Forrest, *Phys. Rev. B* **2011**, *83*, 195326.
[7] Q. Zhang, B. Kan, F. Liu, G. Long, X. Wan, X. Chen, Y. Zuo, W. Ni, H. Zhang, M. Li, Z. Hu, F. Huang, Y. Cao, Z. Liang, M. Zhang, T. P. Russell, Y. Chen, *Nat. Photonics* **2014**, *9*, 35.
[8] B. Kan, M. Li, Q. Zhang, F. Liu, X. Wan, Y. Wang, W. Ni, G. Long, X. Yang, H. Feng, Y. Zuo, M. Zhang, F. Huang, Y. Cao, T. P. Russell, Y. Chen, *J. Am. Chem. Soc.* **2015**, *137*, 3886.
[9] C. Zhou, Y. Liang, F. Liu, C. Sun, X. Huang, Z. Xie, F. Huang, J. Roncali, T. P. Russell, Y. Cao, *Adv. Funct. Mater.* **2014**, *24*, 7538.
[10] L. F. Lai, J. A. Love, A. Sharenko, J. E. Coughlin, V. Gupta, S. Tretiak, T. Q. Nguyen, W. Y. Wong, G. C. Bazan, *J. Am. Chem. Soc.* **2014**, *136*, 5591.
[11] G. C. Welch, L. a. Perez, C. V. Hoven, Y. Zhang, X.-D. Dang, A. Sharenko, M. F. Toney, E. J. Kramer, T.-Q. Nguyen, G. C. Bazan, *J. Mater. Chem.* **2011**, *21*, 12700.
[12] R. Noriega, J. Rivnay, K. Vandewal, F. P. V Koch, N. Stingelin, P. Smith, M. F. Toney, A. Salleo, *Nat. Mater.* **2013**, *12*, 1038.
[13] H. Ade, J.-L. Bredas, J. Carpenter, X. Chen, B. A. Collins, M. Ghasemi, H. Hu, K. Jiang, X. Jiao, J.-H. Kim, J. Y. L. Lai, H. Li, Z. Li, Y. Liu, H. Lin, T. Ma, T. McAfee, T. Wang, H. Yan, L. Ye, J. Zaho, *Submitted* **2017**.
[14] S. Mukherjee, C. M. Proctor, J. R. Tumbleston, G. C. Bazan, T. Q. Nguyen, H. Ade, *Adv. Mater.* **2015**, *27*, 1105.
[15] W. Ma, J. R. Tumbleston, M. Wang, E. Gann, F. Huang, H. Ade, *Adv. Energy Mater.* **2013**, *3*, 864.
[16] Y. H. Liu, J. B. Zhao, Z. K. Li, C. Mu, W. Ma, H. W. Hu, K. Jiang, H. R. Lin, H. Ade, H. Yan, *Nat. Commun.* **2014**, *5*, 1.
[17] S. D. Oosterhout, V. Savikhin, J. Zhang, Y. Zhang, M. A. Burgers, S. R. Marder, G. C. Bazan, M. F. Toney, *Chem. Mater.* **2017**, acs. chemmater.7b00067.
[18] J. Wolf, M. Babics, K. Wang, Q. Saleem, R. Z. Liang, M. R. Hansen, P. M. Beaujuge, *Chem. Mater.* **2016**, *28*, 2058.
[19] Y. Sun, G. C. Welch, W. L. Leong, C. J. Takacs, G. C. Bazan, A. J. Heeger, *Nat. Mater.* **2011**, *11*, 44.
[20] T. S. Van Der Poll, J. A. Love, T. Q. Nguyen, G. C. Bazan, *Adv. Mater.* **2012**, *24*, 3646.
[21] L. Lu, L. Yu, *Adv. Mater.* **2014**, *26*, 4413.
[22] Y. Kim, S. Cook, S. M. Tuladhar, S. A. Choulis, J. Nelson, J. R. Durrant, D. D. C. Bradley, M. Giles, I. McCulloch, C.-S. Ha, M. Ree, *Nat Mater* **2006**, *5*, 197.
[23] K. Forberich, F. Guo, C. Bronnbauer, C. J. Brabec, *Energy Technol.* **2015**, *3*, 1051.
[24] J. Peet, J. Y. Kim, N. E. Coates, W. L. Ma, D. Moses, A. J. Heeger, G. C. Bazan, *Nat Mater* **2007**, *6*, 497.
[25] J. Peet, M. L. Senatore, A. J. Heeger, G. C. Bazan, *Adv. Mater.* **2009**, *21*, 1521.
[26] F. Gao, S. Himmelberger, M. Andersson, D. Hanifi, Y. Xia, S. Zhang, J. Wang, J. Hou, A. Salleo, O. Inganas, *Adv. Mater.* **2015**, *27*, 3868.
[27] R. Steyrleuthner, M. Schubert, I. Howard, B. Klaumunzer, K. Schilling, Z. H. Chen, P. Saalfrank, F. Laquai, A. Facchetti, D. Neher, *J Am Chem Soc* **2012**, *134*, 18303.
[28] M. Schubert, D. Dolfen, J. Frisch, S. Roland, R. Steyrleuthner, B. Stiller, Z. H. Chen, U. Scherf, N. Koch, A. Facchetti, D. Neher, *Adv. Energy Mater.* **2012**, *2*, 369.
[29] J. S. Moon, C. J. Takacs, S. Cho, R. C. Coffin, H. Kim, G. C. Bazan, A. J. Heeger, *Nano Lett.* **2010**, *10*, 4005.
[30] J. A. Love, C. M. Proctor, J. Liu, C. J. Takacs, A. Sharenko, T. S. Van Der Poll, A. J. Heeger, G. C. Bazan, *Adv. Funct. Mater.* **2013**, *23*, 5019.
[31] Y. Y. Liang, Z. Xu, J. B. Xia, S. T. Tsai, Y. Wu, G. Li, C. Ray, L. P. Yu, *Adv. Mater.* **2010**, *22*, E135.
[32] B. A. Collins, Z. Li, J. R. Tumbleston, E. Gann, C. R. McNeill, H. Ade, *Adv. Energy Mater.* **2013**, *3*, 65.
[33] L. J. Richter, D. M. Delongchamp, F. A. Bokel, S. Engmann, K. W. Chou, A. Amassian, E. Schaible, A. Hexemer, *Adv. Energy Mater.* **2015**, *5*, 1.
[34] S. Roland, M. Schubert, B. A. Collins, J. Kurpiers, Z. Chen, A. Facchetti, H. Ade, D. Neher, *J. Phys. Chem. Lett.* **2014**, *5*, 2815.
[35] J. J. van Franeker, M. Turbiez, W. Li, M. M. Wienk, R. a. J. Janssen, *Nat. Commun.* **2015**, *6*, 6229.
[36] F. A. Bokel, S. Engmann, A. A. Herzing, B. A. Collins, H. W. Ro, D. M. DeLongchamp, L. J. Richter, E. Schaible, A. Hexemer, *Chem. Mater.* **2017**, DOI 10.1021/acs.chemmater.6b05358.
[37] L. A. Perez, K. W. Chou, J. A. Love, T. S. Van Der Poll, D. M. Smilgies, T. Q. Nguyen, E. J. Kramer, A. Amassian, G. C. Bazan, *Adv. Mater.* **2013**, *25*, 6380.
[38] S. Engmann, F. A. Bokel, A. A. Herzing, H. W. Ro, C. Girotto, B. Caputo, C. V. Hoven, E. Schaible, A. Hexemer, D. M. DeLongchamp, L. J. Richter, *J. Mater. Chem. A* **2015**, *3*, 8764.
[39] J. Kniepert, M. Schubert, J. C. Blakesley, D. Neher, *J. Phys. Chem. Lett.* **2011**, *2*, 700.
[40] C. M. Proctor, S. Albrecht, M. Kuik, D. Neher, T. Q. Nguyen, *Adv. Energy Mater.* **2014**, *4*, DOI 10.1002/aenm.201400230.
[41] I. A. Howard, R. Mauer, M. Meister, F. Laquai, *J. Am. Chem. Soc.* **2010**, *132*, 14866.
[42] S. Gélinas, A. Rao, A. Kumar, S. L. Smith, A. W. Chin, J. Clark, T. S. van der Poll, G. C. Bazan, R. H. Friend, *Science* **2014**, *343*,

512.
[43] A. A. Bakulin, A. Rao, V. G. Pavelyev, P. H. M. van Loosdrecht, M. S. Pshenichnikov, D. Niedzialek, J. Cornil, D. Beljonne, R. H. Friend, *Science (80-.).* **2012**, *335*, 1340.
[44] H. M. Feier, O. G. Reid, N. A. Pace, J. Park, J. J. Bergkamp, A. Sellinger, D. Gust, G. Rumbles, *Adv. Energy Mater.* **2016**, 1.
[45] G. D'Avino, S. Mothy, L. Muccioli, C. Zannoni, L. Wang, J. Cornil, D. Beljonne, F. Castet, *J. Phys. Chem. C* **2013**, *117*, 12981.
[46] H. Tamura, I. Burghardt, *J. Am. Chem. Soc.* **2013**, *135*, 16364.
[47] L. J. A. Koster, M. Kemerink, M. M. Wienk, K. Maturová, R. A. J. Janssen, *Adv. Mater.* **2011**, *23*, 1670.
[48] R. A. Street, S. Cowan, A. J. Heeger, *Phys. Rev. B* **2010**, *82*, 121301.
[49] Z. Li, F. Gao, N. C. Greenham, C. R. McNeill, *Adv. Funct. Mater.* **2011**, *21*, 1419.
[50] F. Gao, Z. Li, J. Wang, A. Rao, I. A. Howard, A. Abrusci, S. Massip, C. R. McNeill, N. C. Greenham, *ACS Nano* **2014**, *8*, 3213.
[51] A. J. Pearson, P. E. Hopkinson, E. Couderc, K. Domanski, M. Abdi-Jalebi, N. C. Greenham, *Org. Electron.* **2016**, *30*, 225.
[52] Z. Li, G. Lakhwani, N. C. Greenham, C. R. McNeill, *J. Appl. Phys.* **2013**, *114*, DOI 10.1063/1.4813612.
[53] Z. Li, C. R. McNeill, *J. Appl. Phys.* **2011**, *109*, 74513.
[54] C. R. McNeill, I. Hwang, N. C. Greenham, *J. Appl. Phys.* **2009**, *106*, DOI 10.1063/1.3177337.
[55] I. Hwang, C. R. McNeill, N. C. Greenham, *J. Appl. Phys.* **2009**, *106*, DOI 10.1063/1.3247547.
[56] D. Neher, J. Kniepert, A. Elimelech, L. J. A. Koster, *Sci. Rep.* **2016**, *6*, 24861.
[57] S. Albrecht, J. R. Tumbleston, S. Janietz, I. Dumsch, S. Allard, U. Scherf, H. Ade, D. Neher, *J. Phys. Chem. Lett.* **2014**, *5*, 1131.
[58] S. Roland, L. Yan, Q. Zhang, X. Jiao, A. Hunt, M. Ghasemi, H. Ade, W. You, D. Neher, *J. Phys. Chem. C* **2017**, *121*, 10305.
[59] B. A. Collins, H. Ade, *J. Electron Spectros. Relat. Phenomena* **2012**, *185*, 119.
[60] B. A. Collins, J. E. Cochran, H. Yan, E. Gann, C. Hub, R. Fink, C. Wang, T. Schuettfort, C. R. McNeill, M. L. Chabinyc, H. Ade, *Nat. Mater.* **2012**, *11*, 536.
[61] R.-J. J. Roe, *Methods of X-Ray and Neutron Scattering in Polymer Science*, Oxford University Press, New York, NY USA, **2000**.
[62] W. Yin, M. Dadmun, *ACS Nano* **2011**, *5*, 4756.
[63] M. E. Nicho, C. H. García-Escobar, M. C. Arenas, P. Altuzar-Coello, R. Cruz-Silva, M. Güizado-Rodríguez, *Mater. Sci. Eng. B* **2011**, *176*, 1393.
[64] M. B. Isichenko, *Rev. Mod. Phys.* **1992**, *64*, 961.
[65] A. J. Clulow, A. Armin, K. H. Lee, A. K. Pandey, C. Tao, M. Velusamy, M. James, A. Nelson, P. L. Burn, I. R. Gentle, P. Meredith, *Langmuir* **2014**, *30*, 1410.
[66] M. Hambsch, H. Jin, A. J. Clulow, A. Nelson, N. L. Yamada, M. Velusamy, Q. Yang, F. Zhu, P. L. Burn, I. R. Gentle, P. Meredith, *Sol. Energy Mater. Sol. Cells* **2014**, *130*, 182.
[67] B. Warren, *X-Ray Diffraction*, Dover, Mineola, NY, **1990**.
[68] J. Rivnay, R. Noriega, R. J. Kline, A. Salleo, M. F. Toney, *Phys. Rev. B* **2011**, *84*, 45203.
[69] J. A. Bartelt, Z. M. Beiley, E. T. Hoke, W. R. Mateker, J. D. Douglas, B. A. Collins, J. R. Tumbleston, K. R. Graham, A. Amassian, H. Ade, J. M. J. Fréchet, M. F. Toney, M. D. McGehee, *Adv. Energy Mater.* **2013**, *3*, 364.
[70] K. Vakhshouri, D. R. Kozub, C. Wang, A. Salleo, E. D. Gomez, *Phys. Rev. Lett.* **2012**, *108*, 26601.
[71] K. Tvingstedt, K. Vandewal, A. Gadisa, F. Zhang, J. Manca, O. Inganäs, *J. Am. Chem. Soc.* **2009**, *131*, 11819.
[72] C. R. Snyder, R. C. Nieuwendaal, D. M. Delongchamp, C. K. Luscombe, P. Sista, S. D. Boyd, *Macromolecules* **2014**, *47*, 3942.
[73] Y. Han, Y. Guo, Y. Chang, Y. Geng, Z. Su, *Macromolecules* **2014**, *47*, 3708.
[74] J. Liu, M. Arif, J. Zou, S. I. Khondaker, L. Zhai, *Macromolecules* **2009**, *42*, 9390.
[75] A. L. D. Kilcoyne, T. Tyliszczak, W. F. Steele, S. Fakra, P. Hitchcock, K. Franck, E. Anderson, B. Harteneck, E. G. Rightor, G. E. Mitchell, A. P. Hitchcock, L. Yang, T. Warwick, H. Ade, *J. Synchrotron Radiat.* **2003**, *10*, 125.
[76] E. Gann, A. T. Young, B. A. Collins, H. Yan, J. Nasiatka, H. A. Padmore, H. Ade, A. Hexemer, C. Wang, *Rev. Sci. Instrum.* **2012**, *83*, 45110.
[77] J. Rivnay, R. Noriega, J. E. Northrup, R. J. Kline, M. F. Toney, A. Salleo, *Phys. Rev. B* **2011**, *83*, 121306.
[78] M. James, A. Nelson, S. A. Holt, T. Saerbeck, W. A. Hamilton, F. Klose, *Nucl. Instruments Methods Phys. Res. Sect. A Accel. Spectrometers, Detect. Assoc. Equip.* **2011**, *632*, 112.
[79] A. de Juan, R. Tauler, *Anal. Chim. Acta* **2003**, *500*, 195.
[80] A. de Juan, M. Maeder, M. Martínez, R. Tauler, *Chemom. Intell. Lab. Syst.* **2000**, *54*, 123.
[81] J. Jaumot, R. Gargallo, A. de Juan, R. Tauler, *A Graphical User-Friendly Interface for MCR-ALS: A New Tool for Multivariate Curve Resolution in MATLAB*, **2005**.
[82] A. de Juan, R. Tauler, *Crit. Rev. Anal. Chem.* **2006**, *36*, 163.
[83] G. G. Gurzadian, G. Lanzani, C. Soci, T. C. Sum, Eds. , *Ultrafast Dynamics in Molecules, Nanostructures and Interfaces : Selected Lectures Presented at Symposium on Ultrafast Dynamics of the 7th International Conference on Materials for Advanced Technologies, Singapore, 30 June-5 July 2013*, World Scientific Pub. Co, **2014**.
[84] T. M. Clarke, J. R. Durrant, *Chem. Rev.* **2010**, *110*, 6736.
[85] B. Watts, T. Schuettfort, C. R. McNeill, *Adv. Funct. Mater.* **2011**, *21*, 1122.
[86] T. Ferron, M. Pope, B. A. Collins, *Phys. Rev. Lett.***2017**, *119*, 167801.
[87] A. Nelson, *J. Appl. Crystallogr.* **2006**, *39*, 273.
[88] A. Nelson, *J. Phys. Conf. Ser.* **2010**, *251*, 12094.
[89] W. K. Fullagar, K. a Aberdeen, D. G. Bucknall, P. a Kroon, I. R. Gentle, *Biophys. J.* **2003**, *85*, 2624.
[90] D. Deng, Y. Zhang, J. Zhang, Z. Wang, L. Zhu, J. Fang, B. Xia, Z. Wang, K. Lu, W. Ma, Z. Wei, *Nature Communcations*, **2016**, *7*, 13740.
[91] Y. Zhang, D. Deng, Z. Wang, Y. Wang, J. Hang, J. Fang, Y. Yang, G. Lu, W. Ma, Z. Wei, *Advanced Energy Materials*, **2017**, *7*, 1701548.

Mixed domains are found to have a determining role in BHJ solar cells with small-molecule (SM) donors and fullerene acceptors because of their effect on charge generation and percolation. Pure phases, critically important for polymer-fullerene BHJ solar cells, are not required for the local aggregation of SM donors and these can even hinder charge transport between domains. Ring-substituents in SM donors are found to mitigate overall miscibility between donor and acceptor, effectively promoting SM and BHJ solar cell performance via efficient morphologies.

Keywords: Small molecule, organic solar cell, photovoltaic device, charge transport, domain purity, mixed domains, resonant X-ray scattering, microscopy, transient spectroscopy

Obaid Alqahtani, Maxime Babics, Julien Gorenflot, Victoria Savikhin, Thomas Ferron, Ahmed Balawi, Andreas Paulke, Zhipeng Kan, Michael Pope, Andrew J. Clulow, Jannic Wolf, Paul Burn, Dieter Neher, Michael F. Toney, Frédéric Laquai,* Pierre M. Beaujuge,* Brian A. Collins*

Mixed Domains Enhance Charge Generation and Extraction in Bulk-Heterojunction Solar Cells with Small-Molecule Donors

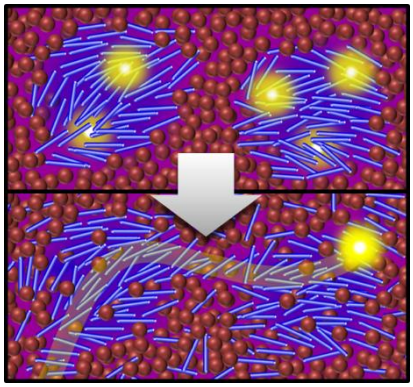

Supporting Information

Mixed Domains Enhance Charge Generation and Extraction in Bulk-Heterojunction Solar Cells with Small-Molecule Donors

Obaid Alqahtani, Maxime Babics, Julien Gorenflot, Victoria Savikhin, Thomas Ferron, Ahmed Balawi, Andreas Paulke, Zhipeng Kan, Michael Pope, Andrew J. Clulow, Jannic Wolf, Paul Burn, Ian R. Gentle, Dieter Neher, Michael F. Toney, Frédéric Laquai, Pierre M. Beaujuge,* Brian A. Collins**

Table of Contents

S1. Device Preparation

The solar cells were prepared on glass substrates with tin-doped indium oxide (ITO, 15 Ω sq^{-1}) patterned on the surface (device area: 0.1 cm^2). Substrates were first scrubbed with dilute Extran 300 detergent solution before immersing in an ultrasonic bath of dilute Extran 300 for 30 min. Samples were rinsed in flowing deionized water for 5 min before being sonicated (Branson 5510) for 20 min each in successive baths of acetone and isopropanol. Next, the samples were dried with pressurized nitrogen before being exposed to a UV−ozone plasma for 20 min. The samples were then transferred into a dry nitrogen glovebox (< 3 ppm O_2) and were placed in a thermal evaporator for an evaporation of a 10 nm thick molybdenum oxide layer evaporated at 0.3 Å s^{-1}; pressure of less than $2x10^{-6}$ Torr. All solutions were prepared in the glovebox using the small molecules synthesized (SM1 & 2) previously and $PC_{71}BM$ purchased from SOLENNE. Optimized devices were obtained by dissolving the small molecules and $PC_{71}BM$ in chlorobenzene, with varying volume concentrations of DIO (0%, 0.2%, 0.5%). Solutions were prepared using a SMx:$PC_{71}BM$ ratio of 1:1 (by weight), with a blend concentration of 30 mg mL^{-1} and were stirred 4 hours at 50 °C before being cast.

The active layers were spin-cast from the solutions at 50 °C at an optimized speed of 800 rpm for 45 s, using a programmable spin coater from Specialty Coating Systems (Model G3P-8), resulting in films of 75 to 85 nm in thickness. The samples were then dried at room temperature for 1 hour. Next, the samples were placed in a thermal evaporator for evaporation of 4 nm thickness calcium layer evaporated at 0.4 Å s^{-1} and 100 nm aluminium electrode evaporated at 5 Å s^{-1}; the pressure in the evaporator was less than $2x10^{-6}$ Torr.

SM	LUMO [eV]	HOMO [eV]	DIO [v.%]	J_{SC} [mA/cm²]	V_{OC} [V]	*FF* [%]	Avg. PCE [%]	Max. PCE [%]
1	3.24	5.05	0	2.1 ± 0.4	0.66 ± 0.02	36 ± 4	0.5 ± 0.1	0.7
			0.2	2.4 ± 0.3	0.66 ± 0.02	42 ± 2	0.7 ± 0.2	0.8
			0.5	5.7 ± 0.3	0.81 ± 0.01	49 ± 2	2.3 ± 0.2	2.5
2	3.23	5.10	0	7.0 ± 0.1	0.95 ± 0.02	36 ± 3	2.4 ± 0.2	2.6
			0.2	10.5 ± 0.2	0.90 ± 0.02	67 ± 2	6.3 ± 0.1	6.5
			0.5	8.2 ± 0.1	0.86 ± 0.01	62 ± 1	4.4 ± 0.2	4.5

Table S1. Molecular energy level information (based on photoelectron spectroscopy in air and absorption onset) and PV performance of SM:$PC_{71}BM$ with different amount of DIO, including deviation across 10 devices.

S2. Absorption Spectroscopy on Devices

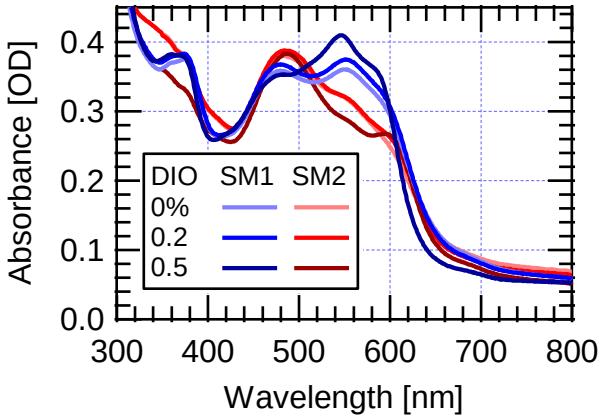

Figure S1: Absorption spectra of device active layers demonstrating the similar level of absorbance for all devices studied in this work.

S3. Transient Absorption Measurement Details

Transient absorption (TA) measurements were performed with a home-built pump-probe setup. Two different configurations of the setup were used for either short delay, namely 100 fs to 8 ns experiments, or long delay, namely 1 ns to 100 μs delays, as described below:

The output of a titanium:sapphire amplifier (Coherent LEGEND DUO, 4.5 mJ, 3 kHz, 100 fs) was split into three beams (2 mJ, 1 mJ, and 1.5 mJ). Two of them were used to separately pump two optical parametric amplifiers (Light Conversion TOPAS Prime), one generating tunable pump pulses, while the second one generating signal (1300 nm) and idler (2000 nm) only. A fraction of the signal of the second TOPAS was focused into a c-cut 3 mm thick sapphire window, thereby generating a white-light supercontinuum from 500 to 1300 nm. The first TOPAS was set to generate 532 nm pulses. While the probe pathway length to the sample was kept constant at approximately 5 meters between the output of the TOPAS and the sample, the pump pathway length was varied between 5.12 and 2.6 m with a broadband retroreflector mounted on a mechanical delay stage (Newport linear stage IMS600CCHA controlled by a Newport XPS motion controller), thereby generating delays between pump and probe from -400 ps to 8 ns.

For the 1 ns to 100 μs delay TA measurement, the same probe white-light supercontinuum as for the 100 fs to 8 ns delays was used, but the excitation light (pump pulse) was provided by an actively Q-switched Nd:YVO4 laser (INNOLAS picolo AOT) frequency-doubled to provide pulses at 532 nm, and triggered by an electronic delay generator (Stanford Research Systems DG535), itself triggered by the TTL sync from the Legend DUO, allowing control of the delay between pump and probe with a jitter of roughly 100 ps.

Pump and probe beams were focused on the sample, which was kept under a dynamic vacuum of $<10^{-5}$ mbar. The transmitted fraction of the white light was guided to a custom-made prism spectrograph (Entwicklungsbüro Stresing) where it was dispersed by a prism onto a 512 pixel NMOS linear image sensor (HAMAMATSU S8381-512). The probe pulse repetition rate was 3 kHz, while the excitation pulses were mechanically chopped to 1.5 kHz (100 fs to 8 ns delays) or directly generated at 1.5 kHz frequency (1 ns to 100 μs delays), while the detector array was read out at 3 kHz. Adjacent diode readings corresponding to the transmission of the sample after excitation and in the absence of an excitation pulse were used to calculate $\Delta T/T$.

Measurements were averaged over several thousand shots to obtain a good signal-to-noise ratio. The chirp induced by the transmissive optics was corrected with a home-built Matlab code by revaluating for each wavelength the delay at which pump and probe are simultaneously arriving on the sample as the time of the signal amplitude. We confirmed the absence of degradation of the samples by repeating the first fluence measurement at the end of the series of fluence dependent measurements.

S4. Multivariate Curve Resolution of TAS Data:

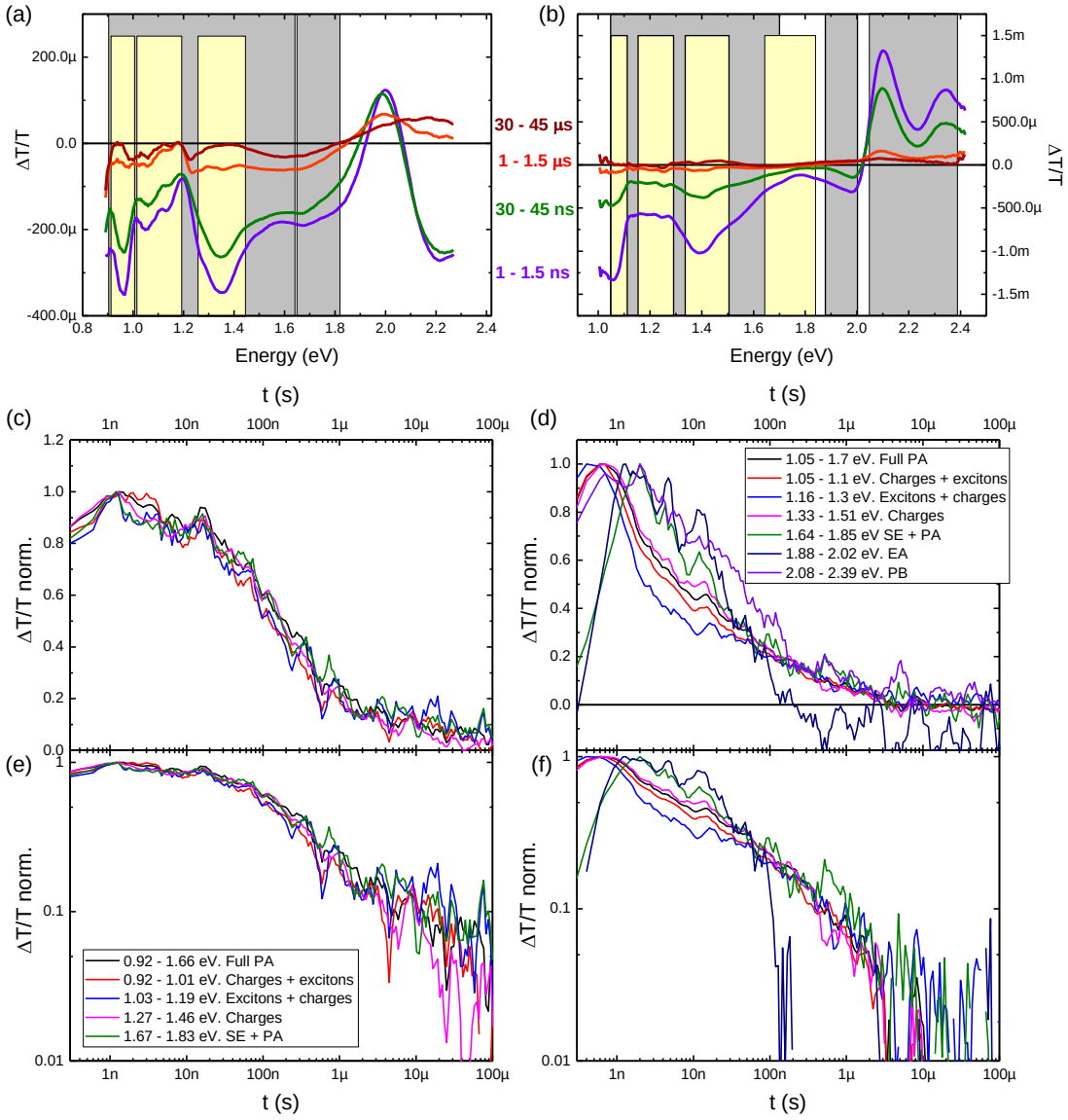

Figure S2: Long delay TA spectra and dynamics of SM2:PC71BM (left column) and SM1:PC71BM (right column) blends. (a) and (b) temporal evolution of the TA spectra. The grey and yellow rectangles represent the features whose kinetics are plotted in semi-logarithmic scale (c) and (d), and log-log scale (e) and (f). The text in the legends of (d) and (e) corresponds to the components/phenomena that contribute to the spectra in the indicated spectral regions. These are: PA = photoinduced absorption, SE = stimulated emission, EA = electroabsorption, PB = photobleach. Note that due to its pronounced shift with time, the photobleach in SM2:PC71BM cannot be confined to a certain spectral range.

As can be seen in Figure S2(c) and Figure S2(e), the whole spectrum in SM2:PC71BM exhibits the same dynamics across the 1 ns to 100 µs time range. The situation is different for SM1:PC71BM (see Figure S2(d) and Figure S2(f)): a quick decay component is present, and have an especially large contribution in the 1.15-1.3 eV region, which is the maximum of excitons absorption in pristine films (see Figure 3). A slow raising component is also present at the transition between the photobleach (PB) and the photoinduced absorption (PA), where electroabsorption (EA) could be expected. The spectral shape of that region, with the pair of peaks of opposite sign peaks at 2 eV and 2.1 eV also suggests the presence of a contribution from electroabsorption, and strongly contrasts with the smoother transition from PB to PA observed in SM2:$PC_{71}BM$. Additionally, we know from measurement in pristine SM2 films (see Figure 3), that excitons possesses spectral feature on the whole studied range (PA from 0.9 to 1.5 eV, stimulated emission and PB from 1.5 to 2.3 eV). As a consequence, charges do not

have any specific absorption range, although they strongly dominate the absorption in the 1.3 – 1.5 eV range.

In order to disentangle these 3 components, we used the free MCR matlab toolbox developed by Tauler et al.[79–82] The details of MCR analysis applied to TA can be found elsewhere.[83] In order to obtain a unique solution, we used the following constraints: the exciton-induced absorption spectrum (extracted from TA of pristine SM1 films) was provided as an input for component 3 and the spectral contribution of component 2 was fixed to zero in the spectral regions distant from the ground state absorption, so that component 2 includes the electroabsorption feature. In order to increase the quantity of data available to the algorithm to extract the individual spectra and thereby to limit the uncertainty, we concatenated the individual data matrices of the 5 studied fluences into one augmented matrix. Finally, as the exciton contribution is expected to be non-negligible only on a very limited temporal region, we separated the data matrix in two submatrices: one for delays between 0 and 10 ns (hereafter named: intermediate delay), for which we considered 3 components, and one for the delays between 3 ns and 100 μs (hereafter named: long delay) for which we considered only 2 components. Furthermore, the 3 ns – 10 ns range was used to check the consistency of the dynamics extracted from the 2 fits.

The spectra of the 3 "intermediate delay" and the 2 "long delay" components as well as the associated kinetics are shown in Figure S3. As can be seen in Figure S3(b) component 3 (whose spectrum was constrained to the exciton-induced absorption spectrum taken from TA experiments on a pristine SM1 film) exhibits typical exciton dynamics often seen in blends. The kinetics of component 1 from "intermediate delay" and "long delay" are virtually the same (see Figure S3(c)). This is the component contributing most to the spectra, and its spectral shape is quite similar to the one and only component observed in SM2:$PC_{71}BM$ optimized blends. Hence, we attribute this component to charges. The charge carrier dynamics used for studying the recombination are obtained by taking the dynamics extracted from the "intermediate delay" MCR for the time range between 0 and 3 ns, the "long delay" MCR for the time range between 10 ns and 125 μs, and the average of those two dynamics for the time range between 3 and 10 ns.

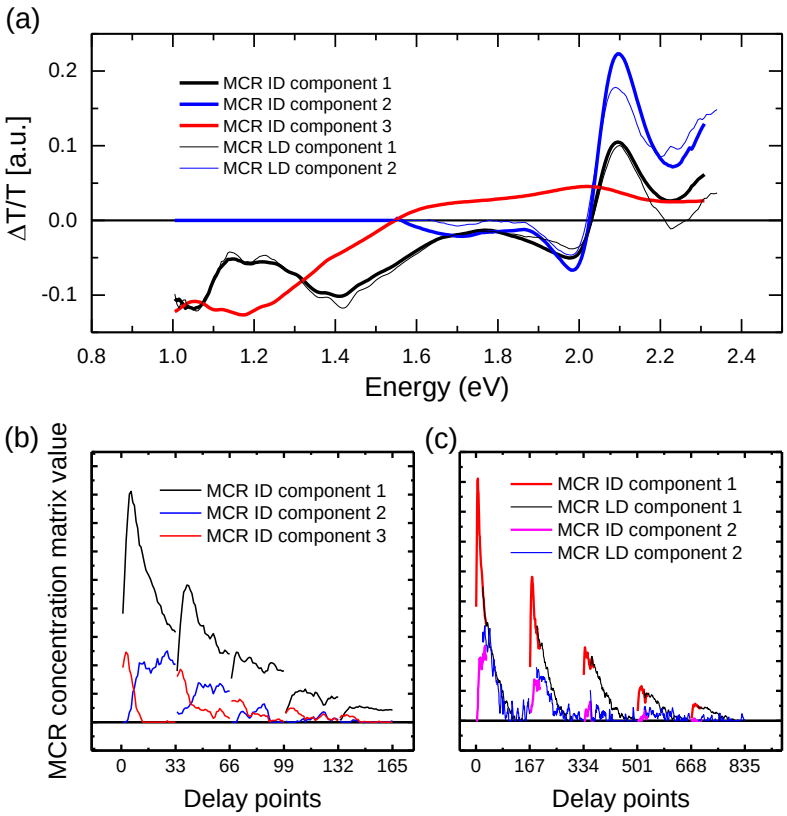

Figure S3: MCR results: (a) spectra of the individual components given as constraints (component 3 in "intermediate delay: ID" MCR and component 2 from 1 to 1.5 eV in both MCR) or extracted by the algorithm. (b) Dynamics of the 3 components for the 5 fluences in "intermediate delay", each fluence has 33 different delays from zero to 10 ns, distributed on a logarithmic scale. (c) Comparison of the dynamics extracted for component 1 and 2 for the "intermediate delay" and the "long delay" time ranges for the 5 fluences; each fluence has in total 166 different delay from zero to 125 µs, distributed on a logarithmic scale with the time range 3 to 10 ns being common to both "intermediate delay" and "long delay" evaluations.

Note that the spectral features assigned to charges comprise their absorption as well as the photobleach they generate, and in addition the electro-absorption signal due to the Stark effect that opposite charge carriers impose on molecules in the ground state located within the transient electric field. The intensity of that third component is not only proportional to the density of charges, but also to the square of the average distance between charges of opposite sign. Its time evolution is thus different from that of the charge carrier density. Here, the electroabsorption feature is partly present in the charge-induced absorption spectrum: namely, the part corresponding to the maximum electron-hole distance found in the course of the decay. The second part of the electro-absorption has its own temporal evolution corresponding to the evolution of the internal field that the molecules in the ground state experience and it has to be taken into account by a third component in the MCR algorithm (here denoted as "component 2"). As we can see in Figure S3(c) the kinetics of the contribution of the electro-absorption in "intermediate delay" and "long delay" are very close, but do not match exactly, more precisely, the contribution is smaller in "intermediate delays". This is most likely a consequence of the fact that a part of the electro-absorption is already included in the charge-induced absorption spectrum, namely the part corresponding to the minimum possible electro-absorption, itself corresponding to the maximum distance between charges of opposite sign that is reached within the considered time range; thus, the component 2 accounts only for the part of electroabsorption that actually varies within this time range. In the "intermediate delay" time range, the average density of charges is larger, as not as much recombination has occurred in this time range, especially at low fluences. As a result, the minimum distance between charges of opposite sign

is smaller and thus the minimum electro-absorption is larger, which implies that a smaller part of the electro-absorption is included in the "variable part" represented by component 2; hence, the smaller contribution of "component 2" in MD compared to LD. Note that even in "long delay", the charge spectrum ("component 1" in MCR) seems to include some contribution of electroabsorption, as seen from the prominent peaks of opposite sign on each side of the onset of the photobleach around 2 eV (note that this is not the case in SM2:PC71BM, see Figure S2). It appears that even though the density of charges is very low and the size of the SM-rich domains should facilitate a separation of charges that diminishes any field between them (see also TEM images),[18] the average distance between opposite charges remains small enough to create electroabsorption. This indicates that even after separation, a significant fraction of charges remains relatively close to the interface, even on a rather large timescale.

S5. Quantification of the density of charges:

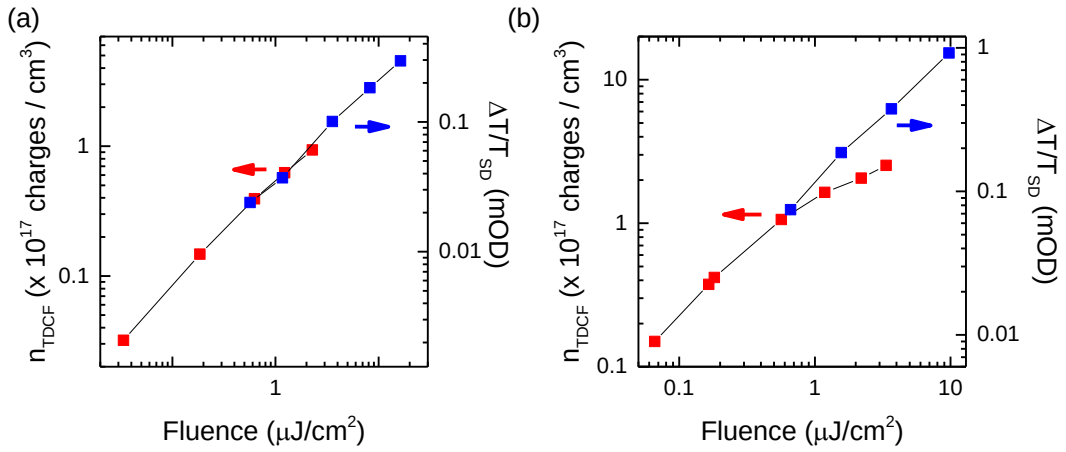

Figure S4: Fluence dependence of the density of charges extracted from TDCF (pump – extract delay of 5 ns) and the average photoinduced absorption (delay: 3.75 – 7.5 ns; energy: 1 – 1.8 eV) for SM1:PC71BM (a) and SM2:PC71BM (b).

In order to quantify the density of charges, we compared the TA signal at a pump - probe delays of 5 ns to the number of charges extracted in a TDCF experiment at a pump – extraction field delay of 5 ns (full charge extraction extending up to 500 ns). For comparison we used the TA data acquired in short delay measurements, because here the pump pulse width is the same as the one used in the TDCF experiment. In SM1:PC71BM, we found a factor of 6.5×10^{-22} cm^3 between the charge density extracted from TDCF and the charge-induced absorption signal averaged between 1 and 1.8 eV (which results in an averaged charge carrier cross section of 6.5×10^{-17} cm^2 in that range for a sample thickness of 100 nm). In SM2:PC71BM, we found a factor of 6×10^{-22} cm^3. Note that the fluence-dependence of the number of charges extracted by TDCF follows closely the trend of the optical signal obtained by TA experiments on SM1:PC71BM, however, this is not the case for SM2:PC71BM, for which the TDCF shows a much more pronounced sub-linear characteristics (see Figure S4). This suggests that additional losses are present in the TDCF experiment. Possible reasons are non-geminate recombination processes assisted by the electrodes as shown recently for a polymer:fullerene blend [Kurpiers, J. & Neher, D. Dispersive Non-Geminate Recombination in an Amorphous Polymer:Fullerene Blend. *Sci. Rep.* **6,** 26832 (2016), which are dependent largely on the morphology and energetics near the contacts Thus we used only the data of the lowest fluence of our TA experiments (0.5 μJ/cm^2 in SM2:PC71BM), for which the non-geminate recombination remains negligible due to the low density of charges.

S6. Parametrization of the charge carrier dynamics by a two-pool model:

Here, we briefly outline the conditions and assumptions used to fit the charge carrier dynamics on the ns-µs timescale using our previously introduced two-pool model:[83]

For each fluence *i* we determined an initial density $n_{0,i}$ of charges from the TA signal amplitude divided by the coefficient determined from comparison with TDCF results (see above). We assume the charges are divided between two pools, namely a density $f \times n_{0,i}$ of spatially-separated charges and a density $(1-f) \times n_{0i}$ of coulombically bound charges, that is, geminate pairs. For these two pools the following rate equations apply.

Coulombically bound charges recombine geminately with an inverse rate constant of τ:

$$\frac{d(1-f)n_i}{dt} = -\frac{(1-f)n_i}{\tau} \quad (1)$$

while spatially-separated charges recombine non-geminately with an apparent recombination order of $\lambda+1$ and a prefactor k_λ:

$$\frac{dfn_i}{dt} = -k_\lambda (fn_i)^{\lambda+1} \quad (2)$$

This yields the following analytical solution used to fit the charge-induced absorption decay at each fluence *i*:

$$n_i(t) = (1-f)n_{0i}\left(1 - e^{-t/\tau}\right) + (\lambda k_\lambda t + (fn_{0i})^{-\lambda})^{-1/\lambda} \quad (3)$$

All fluences are fit simultaneously in a global fit using the shared parameters f, τ, λ and k_λ for all fluences. Note that at low fluence the onset of non-geminate recombination is delayed, so that geminate and non-geminate recombination are sequential instead of parallel and clearly separated by a plateau observed at early times in the charge carrier density dynamics. In that case, each of the parameters can be ascribed to a specific feature of the decay:

- n_0 is naturally the initial signal amplitude;
- τ governs when the first part of the decay occurs (geminate recombination);
- f is the y coordinate of the plateau in a normalized graph (it's the fraction of charges left after geminate recombination is completed);
- k_λ governs the position of the end of that plateau (non-geminate recombination actually sets in around $t = (fn_{0i})^{-\lambda}/\lambda k_\lambda$, but the values of f, λ and n_0 are already determined by other features);
- $-\lambda$ is the asymptotic slope of the decay at long times on a log-log representation.

As a result, there is little capacity for parameters to influence each other. However, at low fluences the poor signal to noise ratio makes the fits ambiguous, whereas at high fluences, geminate and nongeminate recombination are occurring in parallel.[84] Consequently, employing a global fit that uses several fluences enables us to mitigate these problems.
Note that the non-geminate recombination prefactors k_λ extracted for the two materials cannot be directly compared as they are a function of the recombination order λ – see Equation (2). In order to have a comparable value, we reduced the recombination to a bimolecular process and determined the prefactor k_2 by

$$k_2 n^2 = k_\lambda n^{\lambda+1} \quad (4)$$

Using this approach, the value of k_2 depends on the density of charges. In order to get a value relevant for solar illumination conditions, we use a density of charges of $n = n_{1sun} = 5 \times 10^{15}$ cm^{-3} corresponding to the density of charges that can be observed at 1 sun illumination conditions. Thus

$$k_2 = k_\lambda n_{1sun}^{\lambda-1} \quad (5)$$

Table S2. Recombination parameters extracted by using the aforementioned two-pool model.

Film	$n_{0,i}$ [cm^{-3}][a]	f	τ [ns]	$\lambda + 1$	k_2 [cm^3s^{-1}]
SM1:PC71BM	$(1.2 +/- 0.2) \times 10^{18}$ $(7 +/- 2) \times 10^{17}$ $(3.5 +/- 0.6) \times 10^{17}$ $(2.2 +/- 0.4) \times 10^{17}$ $(1.4 +/- 0.3) \times 10^{17}$	0.77 +/- 0.01	1.2 +/- 0.2	2.9 +/- 0.01	$(1.6 +/- 0.7) \times 10^{-12}$
SM2:PC71BM	$(2.4 +/- 0.4) \times 10^{18}$ $(1.5 +/- 0.3) \times 10^{18}$ $(7 +/- 2) \times 10^{17}$ $(3.1 +/- 0.5) \times 10^{17}$ $(2.2 +/- 0.4) \times 10^{17}$	0.87 +/- 0.01	3.8 +/- 0.4	2.6 +/- 0.01	$(1.0 +/- 0.2) \times 10^{-12}$

a. Determined by the charge induced signal amplitude (reconstructed from MCR in the case of SM1, directly measured in the case of SM2) divided by the $n/\Delta OD$ ratio as found from the comparison with the fluence dependent TDCF (see "Quantification of the density of charges" section).

S7. Transient Photocurrent

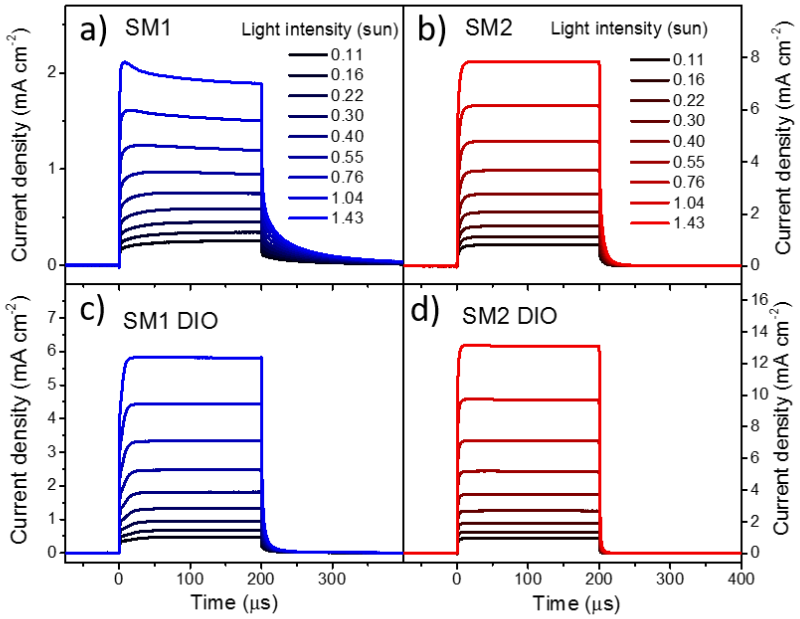

Figure S5: Transient short-circuit current (non-normalized) in response to a 200 µs white light (LED) pulse for (a) non-optimized (no DIO) and (c) optimized (0.5% DIO, v/v) SM1-based BHJ devices, and (b) non-optimized (no DIO) and (d) optimized (0.2% DIO, v/v) SM2-based BHJ devices. The light intensity is given in sun equivalent.

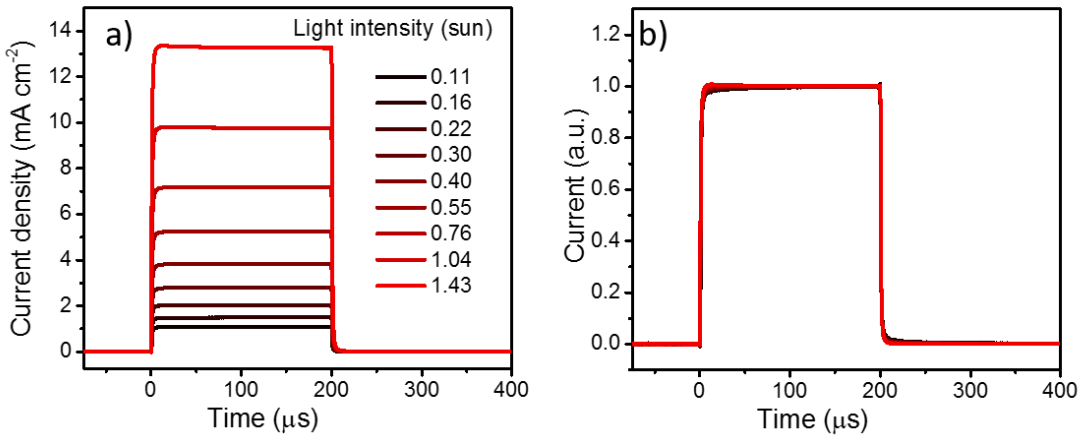

Figure S6: Transient short-circuit current non-normalized (a) and normalized (b) from SM2:$PC_{71}BM$ devices cast from 0.5% DIO showing a slight deterioration of the light intensity dependence relative to ideal devices cast from 0.2% DIO. However, the deterioration is not as drastic as that which occurred in the case of the SM1-blends.

S8. Fit of the JV Characteristics

The JV characteristics of both optimized blends were fitted to Eq. 1 by varying the charge carrier mobility. Values for the non-geminate recombination coefficient k_2 were taken from the TAS data and the layer thickness d was set to 80 nm in both cases. As TDCF showed that the generation efficiency is a function of bias in the SM2 blend, the same bias dependence was used to describe $J_G(V)$ in Eq. 1. For the SM1 blend, TDCF revealed bias-independent charge generation; therefore the generation current was assumed to be constant in the fit of this blend.

The resulting fits are displayed in Figure S7. The SM2 blend can be well described by the given parameters and a mobility of $\mu_{eff} = 4.5\times10^{-5}$ cm^2/Vs, while weak shunting needed to be taken into account to describe the SM1 blend characteristics over the entire bias range.

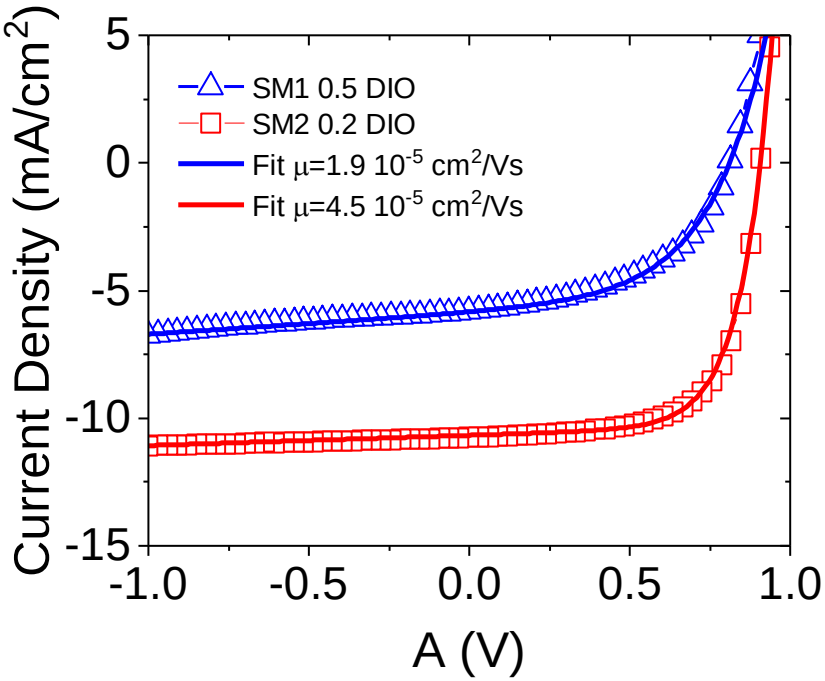

Figure S7: JV characteristics of the optimized devices together with the fit to Eq. 1 .

S9. STXM Measurement of Absolute Domain Composition

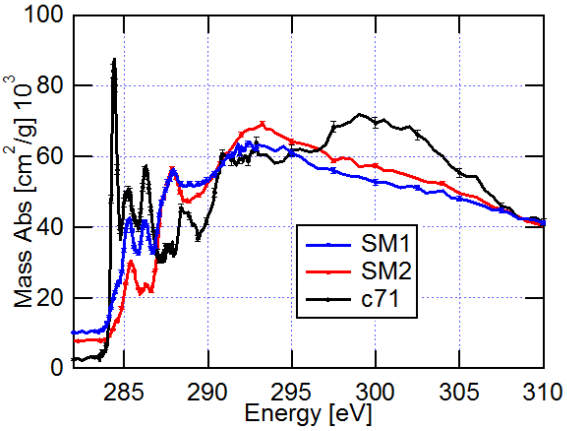

Figure S8: NEXAFS spectra of the three molecules studied in this work ("c71" is $PC_{71}BM$) scaled to bare atom mass absorption coefficient as detailed in Ref 59. The uncertainty comes from counting statistics and accuracy of the data stitched into the bare atom spectrum.

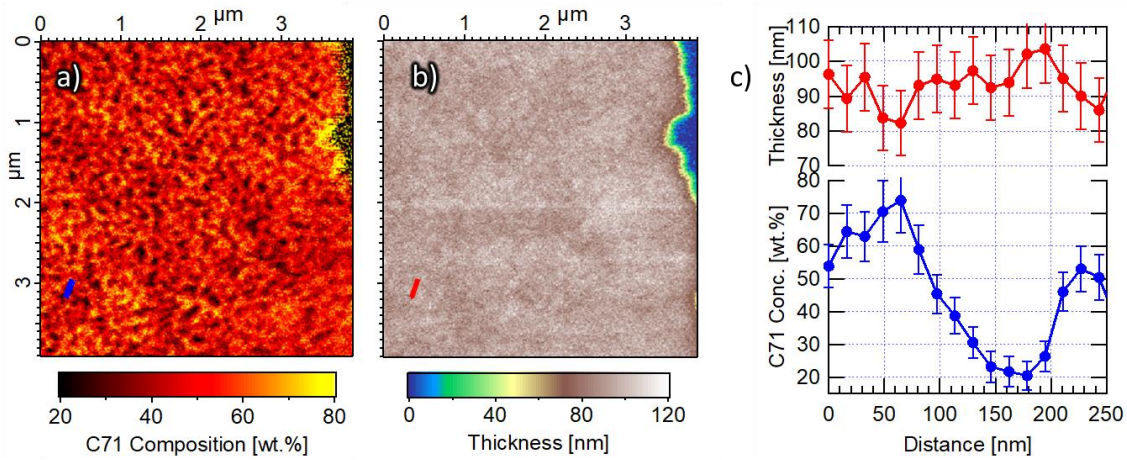

Figure S9: (a). Composition map for SM1:PC71BM processed from CB without DIO additives. (b). Thickness map for the same region as in (a). (c). A composition profile (Blue) extracted from (a) and thickness profile (Red) extracted from (b). Profile locations are marked in their respective colors in (a) and (b). Uncertainties incorporate counting statistics of the two images and uncertainties in the reference spectra (Figure S8).

Figure S9 displays composition and thickness maps for the SM1:$PC_{71}BM$ blends obtained via STXM using photon energies at 284.4 eV and 310 eV. NEXAFS measurements of pure films of each molecule are displayed in Figure S8 and were used to calculate the composition and thickness as detailed in our previous work.[32] Notably for composition in wt.%, densities of the molecules are not needed. However, for the thickness calculation, densities are necessary and the average film density $\rho_{avg} = 1.35 \frac{g}{cc}$ was used based on the NR measurements and the known blend ratio. Dark regions in the composition maps appear to be a dispersed phase with an approximate size of 100 nm and composition of $83 \pm 2\ wt.\%$ SM1. The matrix phase appears to be $30 \pm 3\ wt.\%$ SM1 (70% fullerene). However, the size of these phases indicates that the data is convolved with the STXM beam tails. Our previously published knife-edge test revealed 6.0 ± 0.5 % remaining light from the X-ray beam 100-200 nm away from the edge at the composition-sensitive energy used (284.4eV).[59] For a symmetrical beam and circular domains, this translates into $18 \pm 2\%$ of the beam measuring the matrix phase while it is centered on the dispersed phase. To correct for this, we invert the following system of equations:

$$x'_{1A} = (1-f)x_{1A} + fx_{2A}$$
$$x'_{2A} = fx_{1A} + (1-f)x_{2A}$$

where x'_{1A} is the STXM measured composition of molecule A in domain 1, x_{1A} is the actual composition, and the X-ray beam fraction in the wrong domain $f = 0.18$. Deconvolution results in $x_{1A} = 98 \pm 4\, wt.\%$ and $x_{2A} = 15 \pm 5\, wt.\%$ (all uncertainties propagated). The dispersed domain (domain 1) is likely pure SM1 with the possibility of a thin skin layer of $PC_{71}BM$ on the surface.

S10. Effect of MoOx versus PEDOT:PSS surfaces on morphology

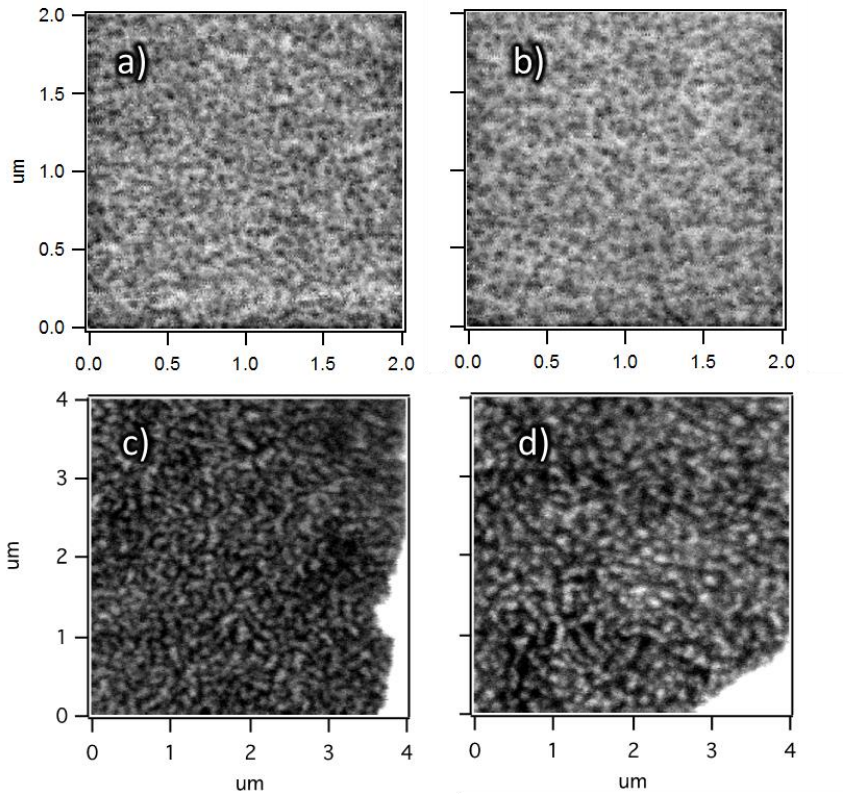

Figure S10: Raw STXM transmission intensities acquired at a photon energy of 284.4 eV for SM1:$PC_{71}BM$ blends. a). Film cast from pure CB on a MoOx/glass substrate. b). Film cast from pure CB on a PEDOT:PSS/glass substrate. c) Films cast from 0.2 v.% DIO on a MoOx/glass substrate. d) Films cast from from 0.2 v.% DIO on a PEDOT:PSS/glass substrate.

Figure S10 shows that the substrate type MoOx/glass or PEDOT:PSS/glass does not significantly affect the lateral mesoscale morphology in SM3:$PC_{71}BM$ processed either from pure CB or CB+0.2 v.% DIO.

S11. Polarized STXM Study of Orientational Domains

STXM is sensitive to molecular orientation when using a photon energy resonant with the C1s-π* transition due to the large dipole moment perpendicular to the aromatic plane of a molecule.[85] We demonstrate this here with films of the liquid crystalline SM2 molecule. In Figure S11a, the film is imaged using a photon energy of 285.4 eV, which is resonant with the π* transition as shown in Figure S8. In this image, domains composed of aligned molecules are revealed. If the same image is acquired at 310 eV as shown in Figure S11b (not resonant with any particular molecular orbital), the film appears uniform indicating that the domains revealed at the former energy are not due to thickness variations. Thus, as we reported earlier, SM2 exhibits liquid crystalline ordering behavior.

A systematic study of molecular alignment in our films is presented in Figure S12 where we compare composition domains in the left column (E=284.4eV) with orientational domains in the right column (E=285.4eV). This study reveals liquid crystalline ordering in both molecular systems which is interesting since as we reported earlier polarized optical microscopy revealed no crystallization of SM1.[18] Comparison with composition domains in the images on the left side are smaller than orientational domains in the images on the right side, but with the SM1 molecule, the orientation persists even in the presence of $PC_{71}BM$ both with and without DIO. Orientational domains in all films are in the range of 0.5-1.5 um in size with SM2 producing smaller domains than SM1. Neither composition nor orientation scans of the SM2:$PC_{71}BM$ blend cast with optimized DIO reveal any structural details due to the resolution limits of STXM.

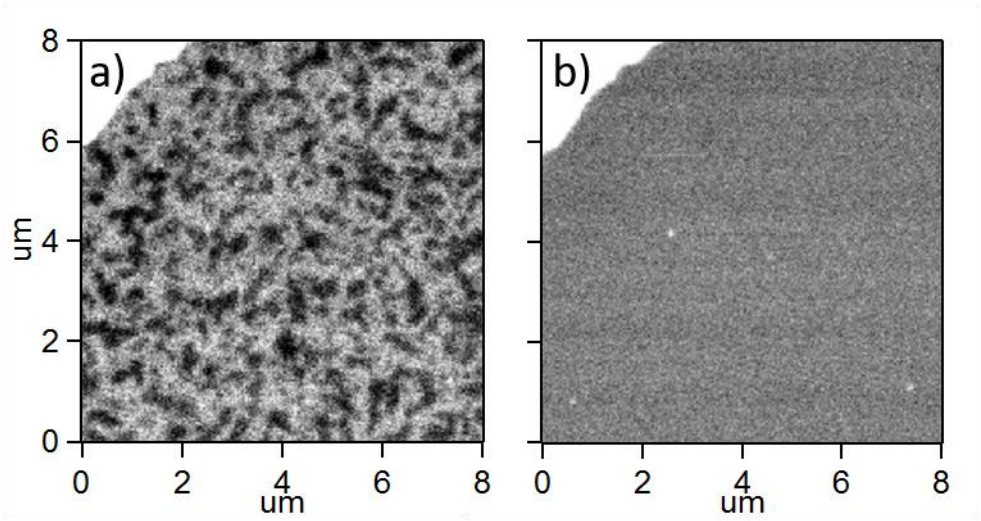

Figure S11: Demonstration of STXM sensitivity to orientation in an SM2 film (cast from pure CB). a) STXM image at 285.4 eV (C1s – π transition). b) STXM image at same location as in a) but with a photon energy of 310 eV (non resonant).*

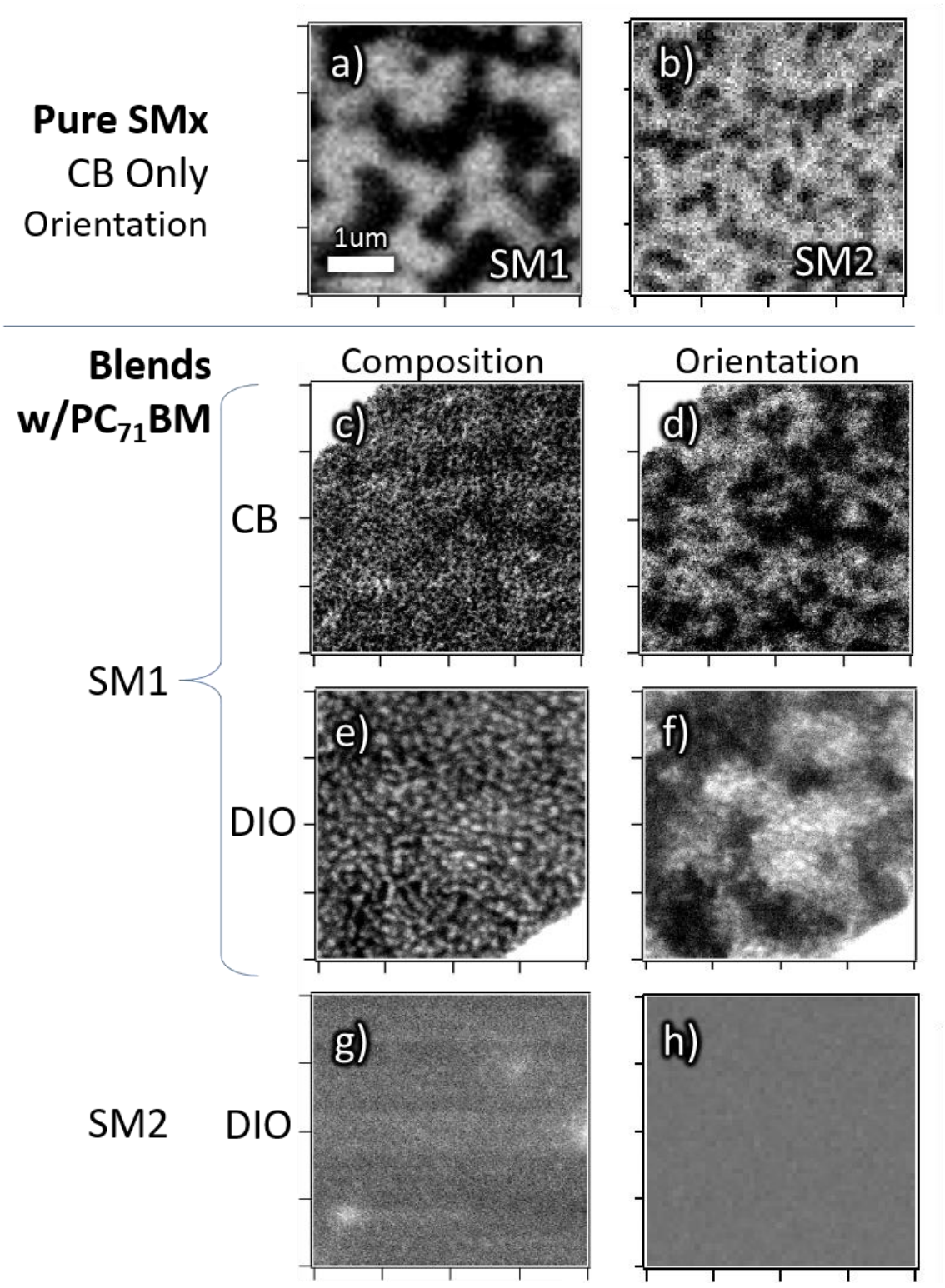

Figure S12: Raw STXM images (detector intensity) for SM1 and SM2 samples at a composition-sensitive energy (E=284.4 eV) or an orientation-sensitive energy (E=285.3 eV – C1s to π), polarization is horizontal. All images are 4um x 4um (see scale bar in (a) and 1um axis ticks). Each tick mark is 1um. (a) Orientation image of pure SM1 processed from CB. (b) Orientation image of pure SM2 from CB. (c) and (d) Composition and orientation images, respectively, of SM1:$PC_{71}BM$ blend processed from CB. (e) and (f) Composition and orientation map, respectively, of SM1:$PC_{71}BM$ blend processed with 0.5 v.% DIO. (g) and (h) Composition and orientation map, respectively, of SM2:$PC_{71}BM$ blend processed with 0.5 v.% DIO. Although no domains or orientation are detected likely due to the 3D nature of the features that are smaller than the STXM resolution.*

S12. Calculation of Domain Composition Fluctuation

Here we calculate the domain compositions of SM1 and SM2 blends films cast without and with optimal DIO concentrations assuming a two domain model. We do this by combining RSoXS measurements with the absolute domain composition measured in STXM on the SM1 blend film cast without DIO. The Porod scattering invariant P can be calculated in two ways

$$P = \int_0^\infty I(q)q^2dq = \frac{8E^4V}{(\hbar c)^4}|\Delta n_{12}|^2\phi_1\phi_2 \quad (6)$$

where $I(q)$ is the scattering intensity, E is the photon energy, V is the scattering volume, $\hbar$ is planck's constant over 2π, c is the speed of light in vacuum, Δn_{12} is the difference in the index of refraction between domains 1 and 2, and ϕ_1 is the volume fraction of domain 1.[61] Here the integral assumes spherical symmetry of the scattering pattern and characterizes the scattering power of a system over all possible length scales of domains. In our case the q-range we have measured covers spectral frequencies from ≈3 nm to ≈1000 nm and is likely sufficient for our molecule materials. However extending the data to higher q-ranges via a power law fit (see Figure S16) does not alter the integrals within 1% precision.

The difference in the index of refraction between domains in Equation (6) can be further separated into the difference of index between the molecules and the composition of each domain: $\Delta n_{12} = \Delta n_{AB}\Delta x_{12}$. Here, Δn_{AB} gives the difference in index of refraction between pure components (labelled A and B) and $\Delta x_{12} = x_{A1} - x_{A2}$ where x_{Aj} is the mass fraction of molecule A in the j^{th} domain.

$$x_{Aj} = \frac{m_{Aj}}{m_{Aj} + m_{Bj}}$$

Where m_{ij} is the mass of the i^{th} material in the j^{th} domain. Therefore, the denominator above gives the total mass of the j^{th} domain. Figure S13a shows our calculation of Δn_{AB} from NEXAFS measurements in Figure S8. The energy indicated in the figure (283.5 eV), is used for this analysis because it is relatively sensitive to composition but insensitive to roughness or orientation fluctuations. The energy is, furthermore, below the absorption edge and thus limits radiation damage and X-ray fluorescence backgrounds.

We measure P through integrating the scattering profiles in Figure 6c. To assure the same scattering volume, we normalize P to film thickness. Film thickness was measured by fitting transmission NEXAFS spectra acquired with the same X-ray beam at the same location on the film used for the scattering experiment. Measurements and fits are shown in Figure S13b. Although the integral for P assumes spherical symmetry of scattering, and thus isotropic domain structure, we know this will not be the case when domain sizes are at or above the film thickness. This is true in the case of the SM1 blends, and reciprocal space scattering is more likely to only have cylindrical symmetry. To correct for this, we measure $I(Q_Z, Q_{XY})$ by tilting the film within the X-ray beam and correcting P for the lower symmetry as was described in our previous publication.[86] The data used for this calculation is displayed in Figure S13c & d showing cylindrical symmetry for the scattering pattern. SM2 blends, having domain sizes well below the film thickness were assumed to scatter in a spherically symmetric pattern.

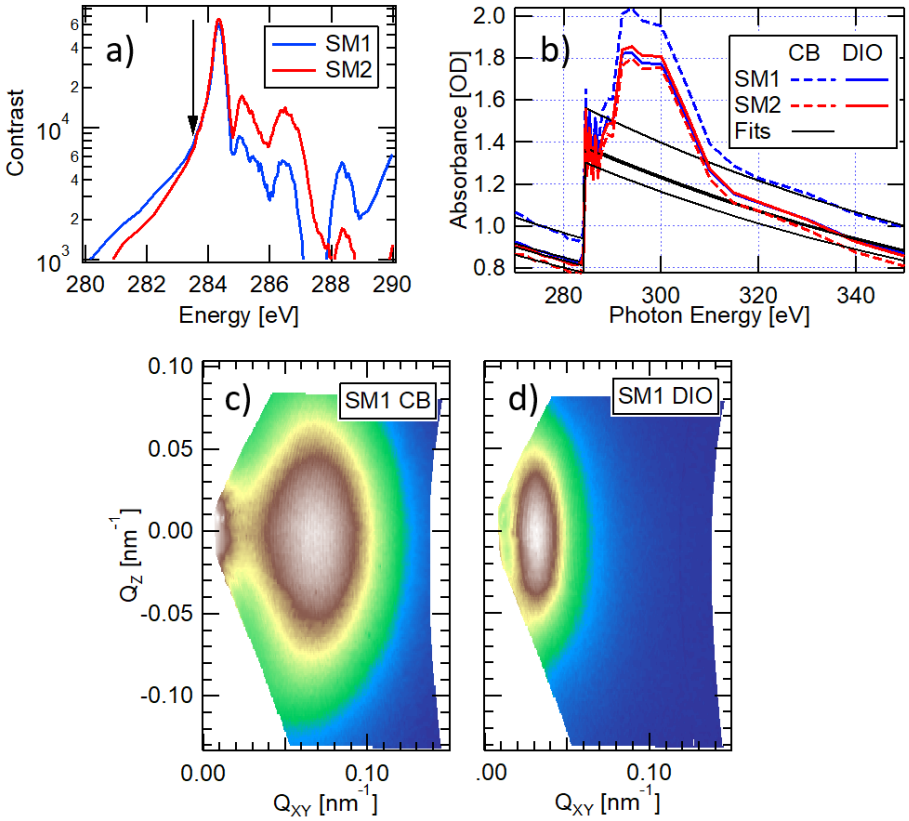

Figure S13: Data used to quantify RSoXS. a) Molecular contrast functions between SMx and PC$_{71}$BM. Densities for each molecule used in this calculation were taken from the NR measurements ($\rho_{SM} = 1.19\ g/cc$, and $\rho_{PCBM} = 1.5\ g/cc$). Arrow represents the energy at which RSoXS data was primarily analyzed. b) NEXAFS absorbance profiles of each film with bare-atom step-edge fits to determine film thickness. Film thicknesses were 98±3 nm and 87±2 nm for SM1 blends without and with 0.5 v.% DIO, respectively. Thicknesses for SM2 blends without and with 0.2 v.% DIO were fit to be 82±3 nm and 88±2 nm, respectively. c) and d) are $I(Q_{XY}, Q_Z)$ reciprocal space maps of scattering (linear color scale) demonstrating cylindrical symmetry of scattering for the SM1 blend films. The data were used to correct for the assumption of spherical symmetry of scattering with $P_C/P_S = 0.905$ for the film without DIO and $P_C/P_S = 1.16$ for the film with DIO.

With the measurements above of P and Δn_{AB}, we can solve Equation (6) for the unknown terms

$$\frac{P}{|\Delta n_{AB}|^2} = C|\Delta x_{12}|^2 \phi_1 \phi_2 \tag{7}$$

Where the unknown scale factor C includes the sample-independent scale factors in Equation (6) as well as unknown experimental factors such as detector efficiency. To determine these remaining unknowns, we use our STXM analysis above and the known mass ratio (R_m) of the two molecules in the film (with total masses M_A and M_B): $R_M = M_A/M_B = 1$ for our 1:1 by weight films. Here the total mass of molecule A can be parameterized as $M_A = m_{A1} + m_{A2} = V_1\rho_1 x_{A1} + V_2\rho_2 x_{A2}$, where V_j is the volume of domain j, and ρ_j is the mass density of domain j. x_{Ai} and m_{ij} are the mass fraction and total mass within a domain as defined previously. SM density was measured through neutron reflectivity to give $\rho_{SM} = 1.19$ g/cc and PC$_{71}$BM density $\rho_{C71} = 1.5$ g/cc. In this analysis we define the domain density as a weighted average comparing the mass density of each component scaled to their weight fraction. Keeping the total mass of each domain conserved, $x_{A1} + x_{B1} = 1$, along with known mass ratio, we can construct the following relationship relating the mass fraction of each domain to their respective phase volumes for a single component.

$$\rho_r \phi_1 x_{A1} + \phi_2 x_{A2} = \frac{R_m}{R_m + 1}(\phi_1 \rho_r + \phi_2) \tag{8}$$

Where we introduce ρ_r as the ratio of densities between domains 1 and 2. Using our STXM analysis of the SM1 blend films cast with optimized DIO we can directly calculate the phase volume fractions for this sample to be 46 v.% pure SM1 and 54 v.% $PC_{71}BM$-rich phase which agrees well with the STXM image itself showing approximately equal areas for each phase. With this knowledge, Equation (7) allows a direct calculation of the scale parameter C allowing a comparison to other samples with domains smaller than the resolution of the STXM through the RSoXS scattering intensity.

Not knowing the exact phase volume for the other samples, we cannot determine with absolute precision, their domain compositions. However, since the scale parameter C is the same for all samples, Δx_{12} as a function of the domain volume fraction can be now calculated for all four films using equation (7) and is plotted in Figure S14a for each film. Since any value is physically possible the bar graph reported in Figure 6d is the average of all possible values with the total range included in the error bars.

The composition of each phase as a function of volume fraction can also be determined by adding together equation (7) and (8) giving the relationship

$$x_{A1} = \frac{1}{2} + \sqrt{\frac{\phi_2}{\phi_1}\frac{P}{C|\Delta n_{AB}|^2}}\left[\phi_1\rho_r + \phi_2\right]^{-1} \tag{9}$$

This information is plotted in Figure S14b. As discussed in the main text we believe a pure small molecule phase is present in all samples (100 wt.% on the y-axis of Figure S14b) with the remaining SM intimately mixed with PCBM. This is due to the diffraction signal from the SM's in GIWAXS as well as the excellent correlation between GIWAXS coherence length and RSoXS domain spacing. In this case, the composition of the other (mixed) domain is equal to Δx_{12}, and the volume fractions for each domain are given by the left-most points from each trace in figure S14b.

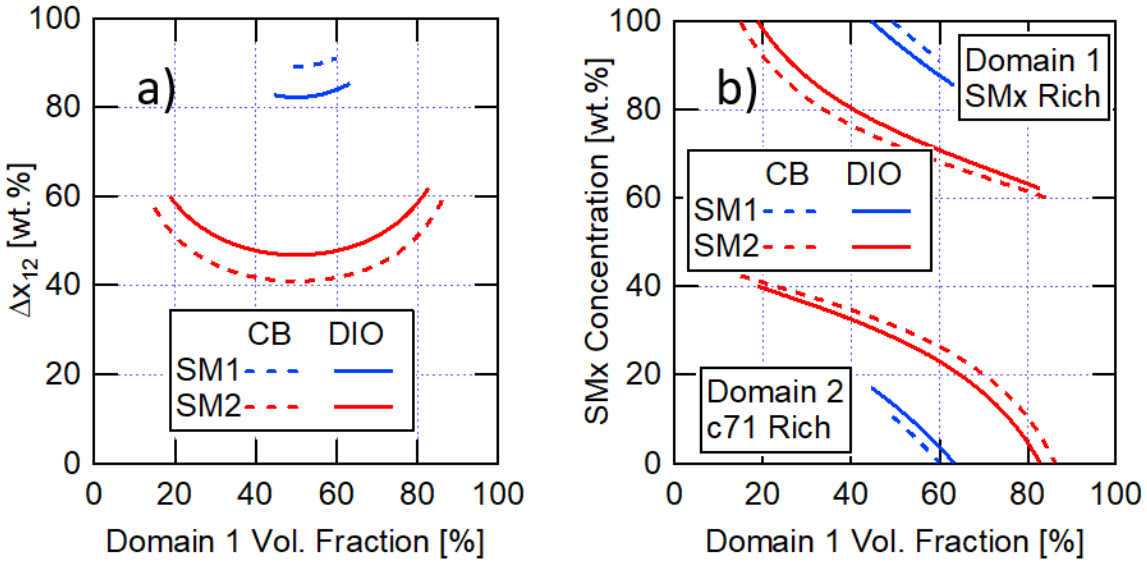

Figure S14: Compositional phase diagram showing all possible domain compositions and volume fractions consistent with the measurements in this work for each of the four samples investigated. As there are three variables (x_{A1}, x_{A2}, and ϕ_1) and only two measurements (TSI and R_m), this analysis alone can only determine the relationship between the parameters. Thus (a) displays the dependence of Δx_{12} on ϕ_1 while (b) displays the dependence of both x_{A1} and x_{A2} on ϕ_1 for all four samples. In (b) the two plots for each sample represent the SM-rich (upper) and SM-poor (lower) domain compositions.

S13. Domain Density and Orientational ordering in RSoXS signals

Comparison of RSoXS profiles at three key energies enables the separation of signals from density, compositional, and orientational domains with the active layers and are displayed in Figure S15. First the red scattering profiles are those presented in the main text and are most sensitive to composition fluctuations (scattering from density and orientation is suppressed). Comparing these profiles to ones acquired at 270 eV (mainly density scattering including surface roughness) demonstrate that the compositional domains of SM1 do have a slight density difference which gives rise to the mirrored domain feature in those traces (see black arrows in the figure). However the 270 eV intensities being ~100 times lower indicates that the density differences are small. In contrast, the same energy comparison for SM2 reveals no mirrored domain feature in 270 eV profiles, demonstrating that compositional domains here have identical densities.

Turning to profiles sensitive to orientational domains (green profiles), it can be inferred that orientational ordering is occurring at spatial frequencies where scattering at 285.4 eV is higher than at 283.5 eV, since 285.4 eV is the energy that directly resonates with the SMx molecule's C1s to π* transition. This transition has a large dipole moment normal to the aromatic plane of the molecule, and so variations in the orientation of this dipole over the distances shown on the top axes will result in increased scattering. In agreement with STXM images of SM1 blends, this enhanced signal of orientational order is present in both films at a lower spatial frequency (larger wavelength) than the composition domains (see green arrows in the figure). For SM2, however, no orientational domains were visible in the STXM. In agreement with this, orientational domains appear to be largely absent from RSoXS of blends without DIO (low Q in Figure S15c where all three traces coincide). However, in SM2-blends with DIO, scattering at 285.4 eV is enhanced at $Q = 0.02\ nm^{-1}$ indicating reemergence of orientational domains with DIO (see green arrow). This result is consistent with measurements of increased aggregation in UV-vis absorbance data shown in Figure 1d and is likely another sign that increased non-crystalline ordering is aiding performance of these devices. The increased scattering at 285.4 eV at high-Q values is confirmed to be from X-ray fluroescence and does not reflect structure in film.

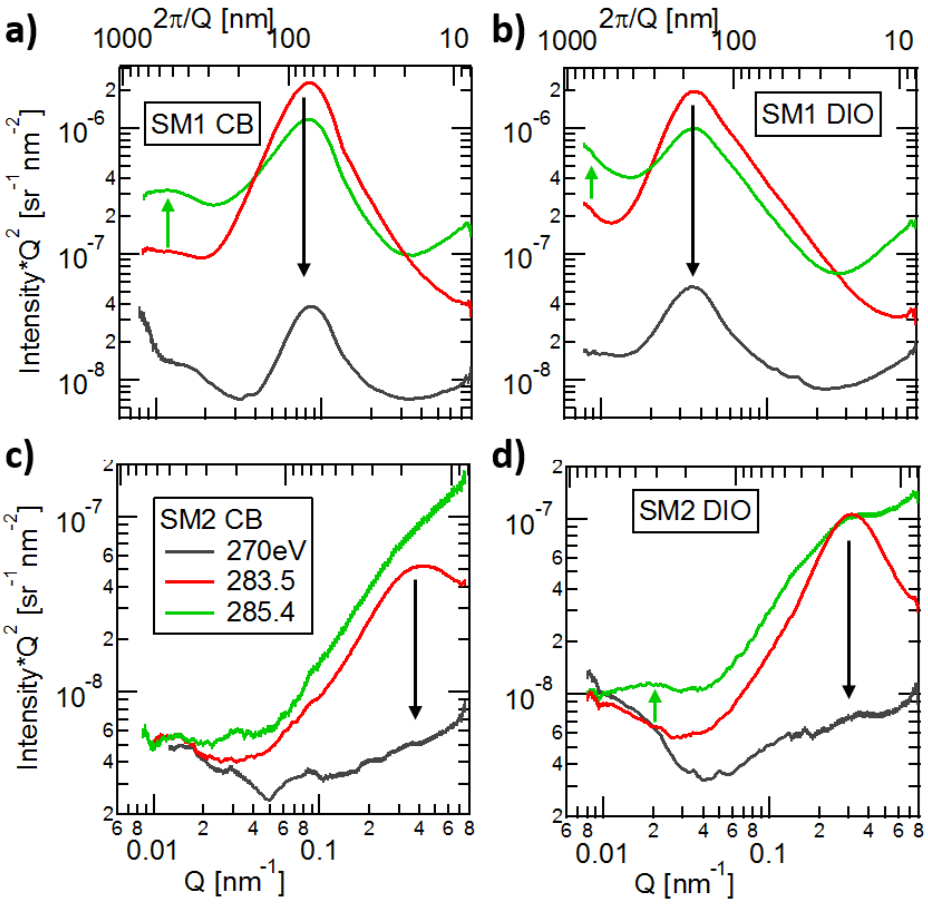

Figure S15: RSoXS profiles at energies maximally sensitive to three different sources of scattering: roughness/density (270 eV, black lines), molecular composition (283.5 eV, red lines), and molecular orientation (285.4 eV, green lines). Arrows are guides to the eye. Profiles for SM1 devices without DIO (a) and with optimized DIO (b). The same arrangement in (c) and (d) for SM2 devices.

S14. Domain Interfaces

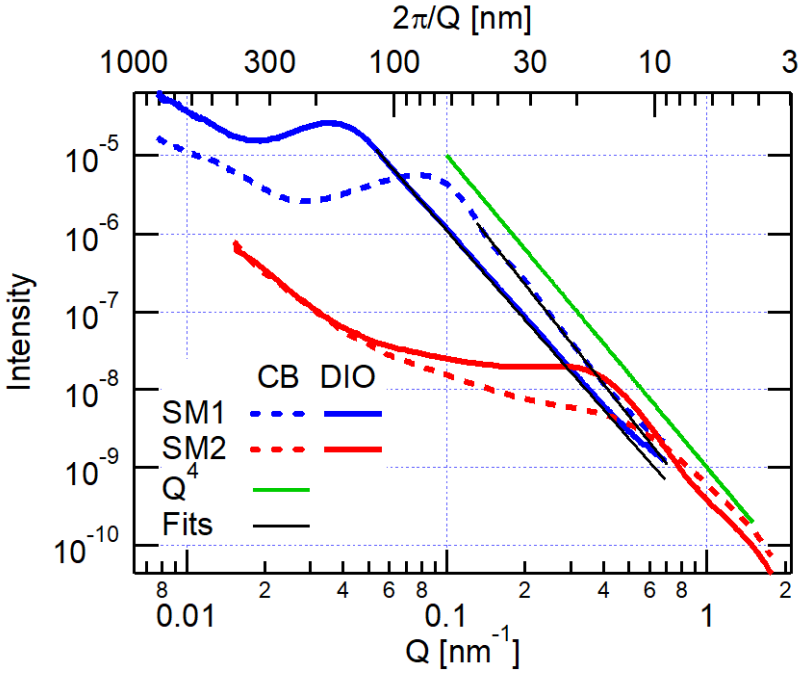

Figure S16: Power law analysis to RSoXS profiles. Fits to SM1 CB result in a power of $p_{CB} = 4.2 \pm 0.1$, while fits to SM1 with optimized DIO result in a power of $p_{DIO} = 3.8 \pm 0.1$. Both are close to the power($p = 4$) associated with smooth and sharp interfaces. SM2 blends don't have enough range after the peak to fit quantitatively.

S15. Neutron Reflectivity

Data Analysis Methods:

The NR data was reduced to give plots of log(Reflectivity) *versus Q* and analysed using the Motofit reflectometry analysis program.[87,88] The NR fits described used an SLD of 2.07×10^{-4} nm^{-2} for the silicon substrate and included a native oxide layer on the surface of the substrate with an SLD of 3.47×10^{-4} nm^{-2}. Mass densities were determined from the modelled SLDs using the SLD calculator built into Motofit. Data were modelled as slabs of different SLDs using the minimum number of layers defined by a thickness, a roughness and an SLD parameter. The neat SMs and MoO_x were fitted as single layers on top of the Si/SiO_2 substrates. The SM2/$PC_{71}BM$ film could be fitted as a two-layer film on top of an $Si/SiO_2/MoO_x$ substrate. The SM1/$PC_{71}BM$ profile could not be reproduced by such simple models and was fitted using the discrete density profiling method.[89] The organic layer was modelled with 20 layers of fixed thickness (4 nm) and roughness (1 nm) and the SLDs of the layers were allowed to vary to determine the vertical SLD profile. SM:$PC_{71}BM$ weight ratios were calculated from the modelled SLDs using a previously reported method.[65] To account for random sample to sample variations, a relative error of ± 5% was ascribed to all modelled SLDs and densities and these errors were propagated throughout the weight ratio calculations.

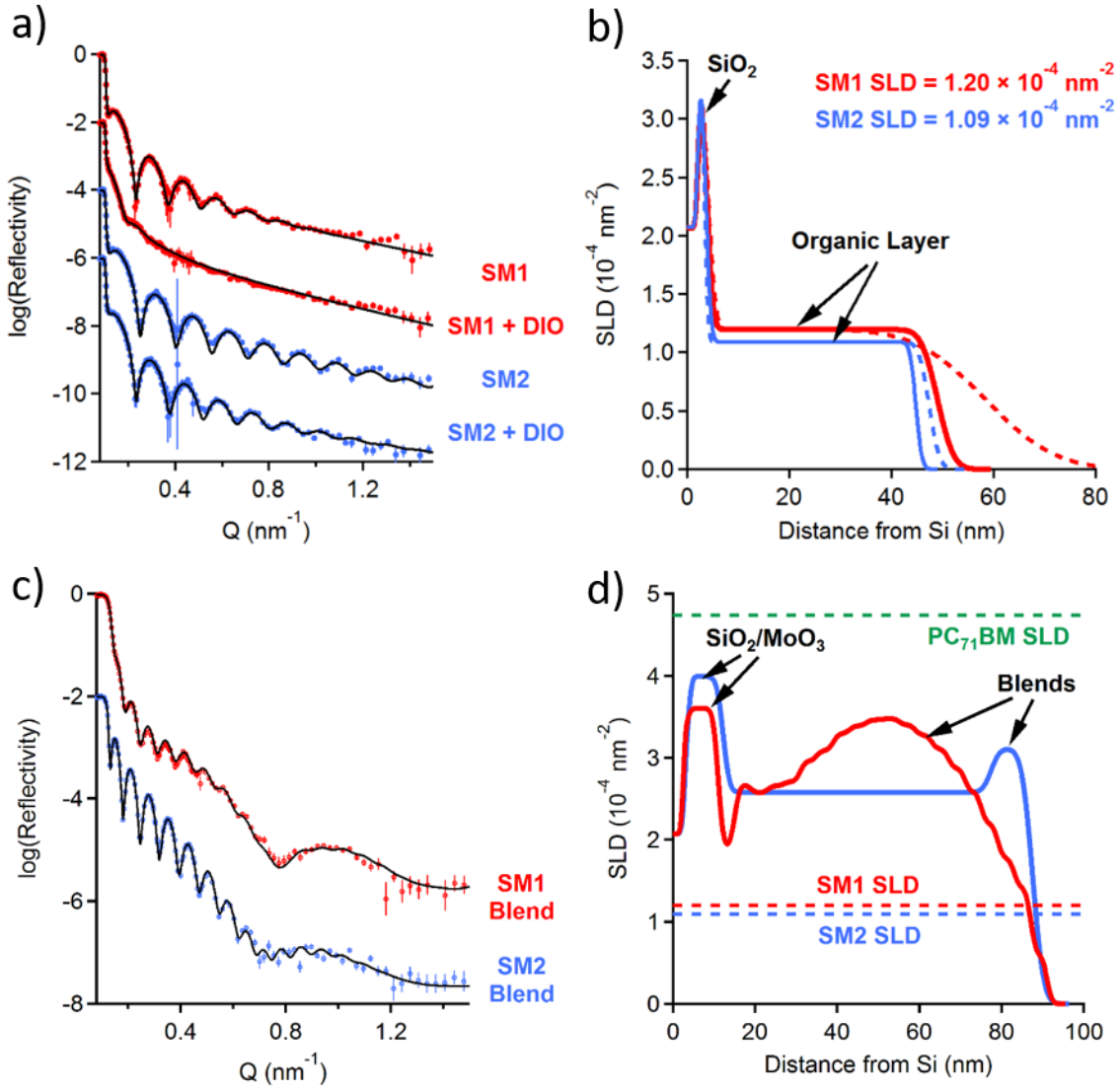

Figure S17: Neutron reflectivity profiles and model fits [a) and c)] and the corresponding SLD versus thickness plots [b) and d)]. Data for SM1 and SM2 spin coated with and without DIO onto silicon wafers are shown in a) and b) and data for the blend systems spin coated with DIO onto silicon wafers coated with a thin layer of MoO_x is shown in c) and d). In a) and c) the traces are offset for clarity, individual points represent recorded data and the solid lines indicate optimized fit curves. In b) the solid lines indicate SMs without DIO and the dashed lines SMs with DIO. In d) the dashed lines indicate the SLDs of the neat materials.

Sample	Substrate	Layer	SLD ($\times 10^{-4}\ nm^{-2}$)
$PC_{71}BM$	Base Si	$PC_{71}BM$	4.74
Neat SM1 from CB and CB+DIO	Bare Si	SM1	1.20
Neat SM2 from CB and CB+DIO	Bare Si	SM2	1.09
SM2:$PC_{71}BM$ blends from CB+DIO	MoOx/Si	Blend (average)	2.67
SM2:$PC_{71}BM$ blends from CB+DIO	MoOx/Si	Blend at surface	3.11
		Blend in bulk	2.85

Table S3: SLD values for layers within each sample measured with Neutron Reflectivity. Values are extracted from the fits shown in Figure S17. *Value for $PC_{71}BM$ is from Reference* [65].

S16. GIWAXS

Grazing Incidence Wide Angle X-Ray Scattering (GIWAXS) experiments were performed at the Stanford Linear Accelerator Center beamline 11-3 with an incidence angle of 0.2° and five 60-second exposures were averaged. For GIWAXS, 60 mg/mL stock solutions of SM1, SM2, and $PC_{71}BM$ in CB were held at 50°C for ~4 hours before being mixed and diluted to a total solids concentration of 30 mg/mL. SM27 and SM28 neat and blend (1:1) films were spin cast at 800 RPM with 800 RPM/s acceleration onto Silicon substrates from chlorobenzene with 0, 0.2%, or 0.5 % DIO by volume. All spin coating was performed in a Nitrogen glovebox. After spin coating, samples were allowed to dry in ambient conditions in the glovebox for over an hour.

Data was calibrated using an LaB6 standard and the Nika/Igor package. Conversion to Qxy/Qz and to Q/Chi was done using a custom script for Igor developed by Stefan Oosterhout.[17] For Scherrer analysis, somewhat isotropic peak at low Q was integrated along χ and fitted to a Gaussian peak on a linear background. The peak width was converted to a coherence length using the Scherrer equation:

$$D = \frac{K\lambda}{B\cos\theta} \quad (9)$$

where D is the coherence length, K is a shape factor taken as 0.94,[67] λ is the X-ray wavelength (12.735 keV = 0.9736 Å), B is the FWHM of the peak, and 2θ is the diffraction angle which is related to Q through Bragg's law.

We also measured a separate batch of films on Si/PEDOT:PSS and on Si/MoOx to check consistency between substrates and between batches. This second set of experiments measured SM1 and SM2 blend films with 0 or 0.5% DIO in the case of SM1 and 0 or 0.2% DIO in the case of SM2. There was good consistency between batches and substrates. All the data is presented in Figure S18.

	SM27:PCBM	SM28:PCBM
0% DIO, Si	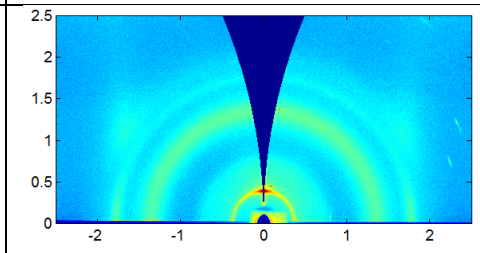	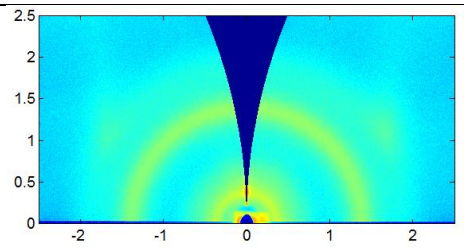
0.2 or 0.5% DIO, Si	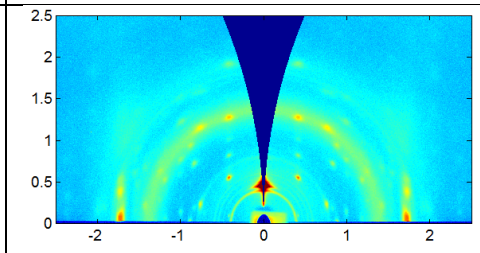	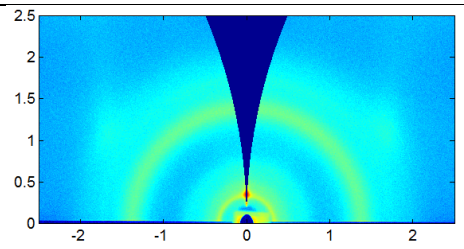
0% DIO, Si/PEDOT:PSS	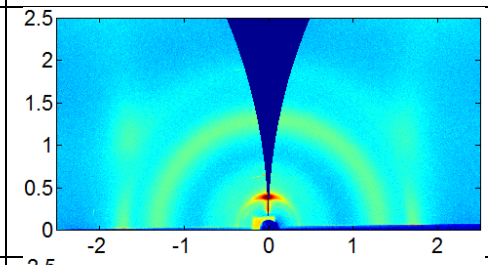	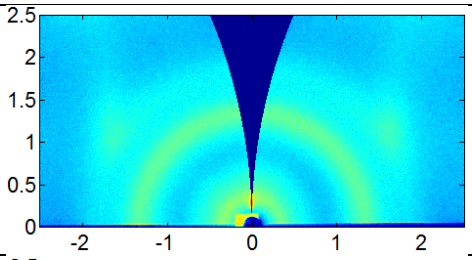
0.2 or 0.5% DIO, Si/PEDOT:PSS	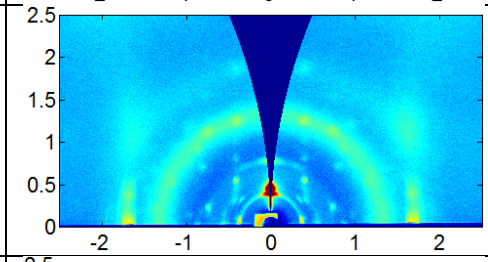	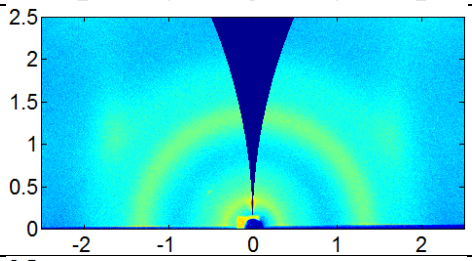
0% DIO, Si/MoOx	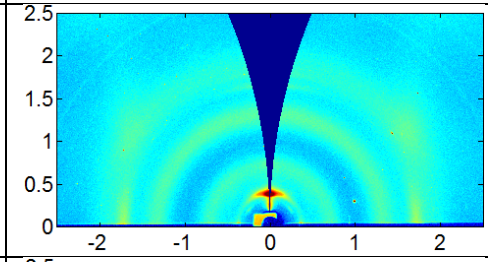	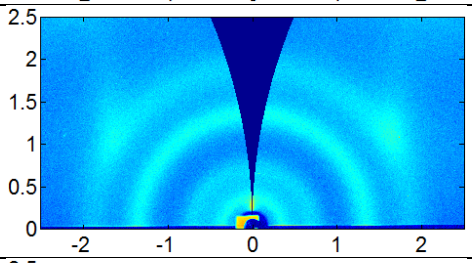
0.2 or 0.5% DIO, Si/MoOx	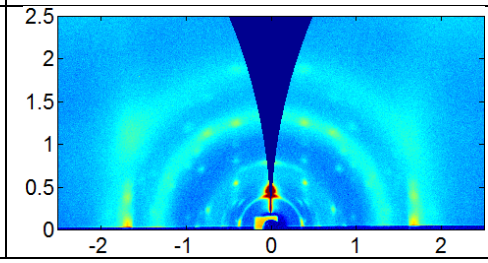	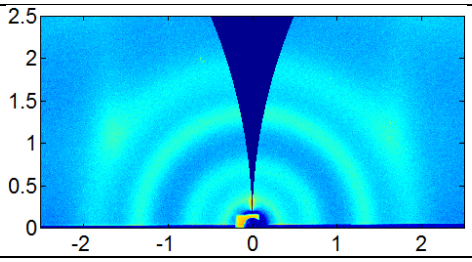

Figure S18: GIWAXS of 1:1 blend materials, with various substrates. SM1:PCBM uses 0.5% DIO and SM28:PCBM uses 0.2% DIO in rows specifying "0.2 or 0.5% DIO". Broad peaks centered at (Qxy,Qz)=(1.64,1.07) Å^{-1} are due to Silicon substrate. PEDOT:PSS gives rise to weak, isotropic scattering rings at Q≈1.23, 1.82 Å^{-1}, and MoOx gives rise to isotropic scattering rings at Q≈0.76, 1.93 Å^{-1}. Similarly, PCBM gives isotropic scattering rings at 0.7, 1.4, and 2.0 Å^{-1}. Total exposure times for samples on Silicon were 300s; all other samples had exposure times of 180s. All data was collected with an incident angle of 0.2°.